

Valtteri Välimäki

CFD SIMULATION OF WIND TURBINE ROTOR AERODYNAMICS AND DROPLET IMPINGEMENT ON BLADES

Master of Science Thesis
Faculty of Engineering and Natural Sciences
Examiners: Visiting Teacher Niko Niemelä
University Lecturer Henrik Tolvanen
January 2023

ABSTRACT

Valtteri Välimäki: CFD simulation of wind turbine rotor aerodynamics and droplet impingement on blades
Master of Science Thesis
Tampere University
Master's Programme in Environmental and Energy Engineering
January 2023

In a transition to more sustainable energy production, wind power has been playing a growing role. It is appealing to build wind farms in the offshore, where there are good wind conditions. The trend is to build turbines with larger swept areas to maximize the power output of one turbine. With longer blades, the blade tip speeds increase as well as the impact speeds of impurities in the air. These impurities can start to erode the blade. Wind turbine leading edge erosion is a significant problem since it affects the aerodynamics of the wing and therefore it has impact on the energy produced. Erosion of the blades also increases the maintenance costs, which can be especially high in the offshore conditions. In this thesis work a water droplet impingement on wind turbine blades is investigated with CFD (Computational Fluid Dynamics) simulations. The main goal is to study droplet trajectories and impact speeds on a wind turbine blade in 2D and 3D simulations and to produce impingement data which can be used in a wind turbine erosion model developed in VTT research center in Finland. The goal is to investigate the differences between 2D and 3D droplet simulations. All the simulations are done with ANSYS Fluent software using a steady state solver.

To ensure the accuracy of the droplet calculations, air flow simulations in 2D and 3D are validated. This is done by comparing simulated results for forces and moments acting on a blade to existing wind tunnel data. The simulation models used in the validation cases are selected based on the models used in similar studies found in literature. After the validation of the simulation results, the droplet trajectories are calculated in the postprocessing of a converged flow solution of 15 MW IEA (International Energy Agency) reference wind turbine (RWT). Droplets are released in the flow field by injections using DPM (Discrete Phase) model.

From the validation cases it can be concluded that the forces and moments can quite accurately be simulated with CFD tools. However, the simulation results compare well with the experimental result only when there is no excessive flow separation from the wing. In the 3D validation cases the simulated torque values of NREL (National Renewable Energy Laboratory) phase VI rotor were in very good agreements with the experimental results with the wind speeds of 7 m/s and 10 m/s with the error percentage of around 5 %. With the wind speeds of 13 m/s and 15 m/s the difference increased to around 25 % due to flow separation. By comparing the impact speeds and trajectories of different sized droplets it can be concluded that the trajectories of bigger droplets behave more like a straight line whereas smaller droplets are adapted by the surrounding flow nearly instantly. The difference between in 2D and 3D simulations was that the impact speeds of droplets were lower in 3D simulation than in 2D simulation. The difference was emphasized with smaller droplets. For future work, the reasons behind the different impact speeds in 2D and 3D simulations could be studied. Also, different particle diameters and densities could be investigated.

Keywords: CFD, DPM, impingement, validation

The originality of this thesis has been checked using the Turnitin OriginalityCheck service

TIIVISTELMÄ

Valtteri Välimäki: Tuuliturbiinin roottorin aerodynamiikan CFD mallinnus ja pisaroiden iskeytyminen lapoihin
Diplomityö
Tampereen Yliopisto
Ympäristö- ja energiatekniikan diplomi-insinöörin tutkinto-ohjelma
Tammikuu 2023

Tuulivoiman rooli tulee kasvamaan merkittävästi siirryttäessä kohti hiilineutraalia energiantuotantoa. Tuulipuistoja on rakennettu perinteisesti maalle, mutta kiinnostus merituulivoimaloita kohtaan on kasvussa houkuttelevien tuuliolosuhteiden vuoksi. Tuuliturbiinien kokoa pyritään kasvattamaan, jotta yhden turbiinin tuottamaa tehoa saadaan maksimoitua. Lapojen pituutta kasvatettaessa, lavan kärjen nopeus kasvaa, jonka vuoksi myös lapaan osuvien partikkeleiden törmäysnopeudet kasvavat. Ilmassa olevat partikkelit voivat olla esimerkiksi vesipisaroita, jääkiteitä tai hiekkaa ja ne voivat alkaa kuluttamaan lavan pintaa. Tuuliturbiinin lavan eroosio on merkittävä ongelma, sillä se vaikuttaa lavan aerodynamiikkaan ja siten myös tuotetun energian määrään. Eroosion aiheuttamien ongelmien korjaaminen kasvattaa myös huoltokustannuksia, jotka voivat olla erityisen korkeita merituulivoimaloissa. Tässä työssä tarkastellaan vesipisaroiden iskeytymistä tuuliturbiinin lapoihin CFD ohjelmistolla. Työn päätavoitteena on tutkia pisaroiden lentoratoja ja törmäysnopeuksia tuuliturbiinin lapoihin 2D ja 3D simulaatioissa, sekä verrata tuloksia keskenään. Tavoitteena on tuottaa dataa, jota voidaan käyttää hyödyksi VTT:llä kehitetyssä eroosiomallissa. Kaikki simulaatiot on tehty ANSYS Fluent ohjelmistolla aikariippumattomana laskentana.

Jotta mahdollisimman tarkat pisaramallinnukset saataisiin tehtyä, 2D ja 3D simulaatiot validoidaan, vertaamalla lapaan vaikuttavia voimia ja momentteja tuulitunnelissa mitattuihin kokeellisiin arvoihin. Simulaatioissa käytetyt mallit valitaan kirjallisuudesta löytyvien vastaavien tutkimusten pohjalta. Validoinnin jälkeen lasketaan pisaroiden liikeradat ja törmäysnopeudet. Näiden laskemisessa käytetään IEA-15-240 referenssiturbiinin konvergoitunutta virtauskenttää. Pisarat vapautetaan virtauskenttään injektioina käyttäen DPM mallia.

Validoinnin tuloksena voidaan vetää johtopäätös, että käytetyillä malleilla voidaan melko tarkasti mallintaa lapaan vaikuttavia voimia ja momentteja. Tulokset ovat kuitenkin tarkkoja ainoastaan olosuhteissa, joissa virtaus ei irtoa siivestä. 3D simulaatioiden validoinnin tuloksena saatujen vääntömomenttien arvot vastasivat erittäin hyvin kokeellista dataa, eron ollessa noin 5 % tuulen nopeuksilla 7 m/s ja 8 m/s. Tuulennopeuksilla 13 m/s ja 15 m/s erot kokeelliseen dataan nousivat merkittävämmäksi, noin 25 prosenttiin. Lentoratoja ja törmäysnopeuksia vertaamalla voidaan vetää johtopäätös, että isommat pisarat käyttäytyvät melko suoraviivaisesti virtauskentässä, kun taas pienemmät pisarat mukautuvat ympäröivään virtaukseen lähes välittömästi. 2D ja 3D simulaatioiden erona oli, että törmäysnopeudet olivat pienempiä 3D simulaatiossa ja erot korostuivat pienemmillä pisaroilla. Tulevaisuudessa syitä eri törmäysnopeuksille 2D ja 3D simulaatioiden välillä voitaisiin tutkia tarkemmin. Lisäksi pisaramallia voitaisiin laajentaa useammalle eri partikkelin halkaisijalle ja tiheydelle.

Avainsanat: CFD, DPM, validointi

Tämän julkaisun alkuperäisyys on tarkastettu Turnitin OriginalityCheck -ohjelmalla.

PREFACE

I would like to express my gratitude to my supervisors Raul Prieto for giving me a change to work on this topic and being supportive throughout the entire process and Niko Niemelä for introducing me to CFD and for supporting me especially in the writing of the thesis. I would also like to thank my family and friends.

Tampere, January 11, 2023

Valtteri Välimäki

TABLE OF CONTENTS

1.INTRODUCTION	1
2.WIND POWER AND RAIN INDUCED EROSION.....	3
2.1 Concept of wind energy	3
2.2 Characteristics of airflow around wind turbines	5
2.3 Forces and moments acting on wind turbine blade	6
2.4 Rain droplet impingement and blade erosion	10
3.SIMULATION OF AIRFLOW AND WATER DROPLET IMPINGEMENT	13
3.1 Governing equations for airflow around wind turbines	13
3.2 Modelling turbulence	16
3.3 Simulating rotation of the wind turbine blades	18
3.4 Simulating water droplets in airflow	19
4.MATERIALS AND METHODS	22
4.1 Workflow	22
4.2 Validation of 2D and 3D simulations.....	23
4.3 Reference wind turbine IEA-15-240	27
4.4 Modelling impingement of water droplets on blades	28
5.RESULTS AND DISCUSSION.....	32
5.1 Results for validation of 2D simulation.....	32
5.2 Results for validation of 3D simulations.....	35
5.3 Results for IEA-15-240-RWT.....	40
5.4 Droplet impact speeds and comparison of 2D and 3D results	41
6.CONCLUSIONS AND FUTURE WORK.....	45
REFERENCES.....	47

TABLE OF FIGURES

Figure 1. Stream tube concept. [5].....	3
Figure 2. Actuator disc concept. [5].....	4
Figure 3. Stagnation point and streamlines of airflow over airfoil.....	6
Figure 4. Performance curve. [5].....	8
Figure 5. Airfoil geometry. [10].....	8
Figure 6. Forces acting on an airfoil. [11].....	9
Figure 7. Rain droplet diameter probability density with different rain intensities. [14].....	11
Figure 8. Droplet terminal velocity as a function of droplet diameter. Data from Ref. [15].....	12
Figure 9. Rotating reference frame with periodic boundaries. Adapted from Ref. [18].....	19
Figure 10. Particle trajectory in 2D domain.	20
Figure 11. Droplet trajectory in a rotating reference frame with periodic boundaries.	20
Figure 12. Workflow for the thesis research.	22
Figure 13. Full calculation domain (left) and close-up view around the airfoil (right).	23
Figure 14. The entire calculation domain (right), and closer view on the blade in the middle of the domain (left).	25
Figure 15. NREL phase VI blade with span wise sections.....	26
Figure 16. Entire calculation domain (left), blade in the middle of the domain (right).	27
Figure 17. Droplet trajectories with impacts on the entire length of leading edge.	29
Figure 18. Droplet trajectories in 3D domain with droplets impacting the entire length of leading edge.....	30
Figure 19. Mesh independence study.	32
Figure 20. Moment coefficient as a function of angle of attack.....	33
Figure 21. Drag coefficient as a function of angle of attack.....	34
Figure 22. Lift coefficient in a function of angle of attack.....	34
Figure 23. Span wise locations of NREL phase VI blade.	35
Figure 24. Local normal force coefficients [-] as a function of wind speed [m/s] for different span wise positions.	36
Figure 25. Local normal force coefficient [-] (top) as a function of span wise position. Local dynamic pressure [Pa] (bottom) as a function of span wise position with wind speeds 7 m/s and 10 m/s.....	37
Figure 26. Contours of turbulent kinetic energy in the span wise locations of the wing.	38
Figure 27. Torque as function of wind speed.	39
Figure 28. Average impact speed relative to upstream velocity as a function of droplet diameter.	42
Figure 29. Comparison of positions of maximum impact velocity positions in 2D and 3D simulations with different diameter droplets. Droplet diameter in mm. (2D impact position on top and 3D below).....	43
Figure 30. Velocity contours of 2D simulation (left) and the 3D simulation (right) at the radial position of impingement.....	44

LIST OF ABBREVIATIONS AND SYMBOLS

BEM	Blade Element Momentum theory
CFD	Computational Fluid Dynamics
DNS	Direct Numerical Simulation
DPM	Discrete Phase Model
FVM	Finite Volume Method
IEA	International Energy Agency
LES	Large Eddy Simulation
NREL	National Renewable Energy Laboratory
RANS	Reynolds Averaged Navier Stokes
RSM	Reynolds Stress Model
RWT	Reference Wind Turbine
SIMPLE	Semi Implicit Method for Pressure Linked Equations
SST	Shear Stress Transport
α	Angle of attack ($^{\circ}$)
γ	Ratio of specific heats (-)
γ_d	Terminal velocity of droplet (m/s)
Γ	Diffusion coefficient (m^2/s)
Γ_k	Effective diffusion term for k (m^2/s)
Γ_{ω}	Effective diffusion term for ω (m^2/s)
δ	Boundary layer thickness (m)
ε	Dissipation rate of turbulent kinetic energy ($J/kg^{-1} s^{-1}$)
λ	Tip speed ratio (-)
μ	dynamic viscosity ($J/kg^{-1} s^{-1}$)
ν	Kinematic viscosity (m^2/s)
ρ	Density (kg/m^3)
Ψ	Azimuthal angle of blade ($^{\circ}$)
ω	Turbulent frequency (1/s)
Ω	Rotor rotational speed (rad/s)
A	Rotor swept area (m^2)
C_d	Drag coefficient (-)
C_l	Lift coefficient (-)
C_p	Power coefficient (-)
C_Q	Torque coefficient (-)
C_T	Thrust coefficient (-)
D	Drag (N)
K	Heat Conduction ($W m^{-1}K^{-1}$)
L	Lift (N)
Ma	Mach number (-)
P	Power (W)
Q	Torque (Nm)
R_u	Gas constant ($J mol^{-1} K^{-1}$)
R	Radius of the rotor (m)
Re	Reynolds number (-)
S	Reference area (m^2)
T	Temperature of the air flow (K)
T_r	Rotor thrust (N)
T_0	Stagnation temperature (K)
U_{∞}	Wind speed (m/s)
U_{flow}	Air flow velocity relative to the blade velocity (m/s)
W_g	Droplet velocity relative to the ground (m/s)

W_b	Droplet velocity relative to the blade velocity (m/s)
a	Axial induction factor (-)
a_s	Speed of sound (m/s)
k	turbulent kinetic energy (J/kg)
p	Pressure of the airflow (Pa)
p_0	Stagnation pressure (Pa)
q_∞	Dynamic pressure (Pa)
r	Radial position of droplet impact (m)
t	time (s)
u	velocity component (m/s)
u_t	Blade tip speed (m/s)
y^+	Dimensionless wall distance (-)

1. INTRODUCTION

In a transition to more sustainable energy production, interest towards wind energy is rapidly rising. In 2021, electricity generated by wind power increased 17 % [1]. The trend is to build taller wind turbines with longer blades. The blade tip speed in modern wind turbines can reach a velocity of 100 m/s, causing substantial erosion problems [2]. With these high velocities, the particles in the air impacting the blade cause a substantial problem. The impurities (sand, ice, droplets etc.) start to deform the blade, usually made from fiber glass or carbon fiber reinforced plastics [3]. Erosion increases the surface roughness, which affects the aerodynamics of the blade. Erosion in offshore wind turbines is especially problematic, because they operate in harsh conditions and have high maintenance costs. [2]. It has been estimated by Sareen et al. [4] that depending on the severity of the erosion, the loss in annual energy production can be up to 25 %. The life span of a wind turbine is about 25 years, and it has been studied that the erosion can start as soon as within few years after installation [1].

Computer simulations are extensively used in modern wind turbine research and development. Different models have been developed for estimating the erosion rates of the blades. To get reliable estimations of the erosion, characteristics of rain droplet trajectories and velocities are needed. The droplet movement in the airflow can be simulated using CFD (Computational Fluid Dynamics) tools. To accurately model the movement of droplets, accurate simulation of the flow field around the blade is needed. To estimate the accuracy of the simulations, the simulation results of forces and moments acting on a wind turbine blade can be compared with an experimental wind tunnel test.

The goal of this work is to simulate the trajectories and the impact speeds of droplets impinging on wind turbine blades. With the accurate droplet trajectory and impact simulations, more reliable erosion models can be made. 2D and 3D simulation results are validated first by comparing the forces and moments acting on a blade to experimental values. The research questions for this thesis work are:

1. What are the wind turbine rotor aerodynamic properties and how they are connected to the droplet impingement and erosion of the blades?

2. What are suitable sub models and simulation strategies for capturing the rotor aerodynamics and droplet impingement, considering the accuracy and computational cost point of view?
3. How accurately do the simulated aerodynamics of FFA-W3-211 airfoil and NREL phase VI rotor compare with wind tunnel test data?
4. What are the trajectories and impact speeds of droplets impinging on the IEA-15-240-RWT blade and how the results compare between 2D and 3D simulations?

In Chapter 2 the theory of wind turbines and characteristics of airflow over blades and the erosion of the blades are discussed. The first research question is answered in this chapter based on literature. Third Chapter is the theory chapter for the simulation methods of modelling wind turbines. In this chapter, the governing equations for airflow and turbulence models are discussed. Also, the methods for modelling the rotation of blades, and the droplet impingement are discussed. In this chapter, the suitable models for this work are selected. In the fourth chapter, the materials and methods for this work are presented. The used models and calculation grids are presented. In the fifth chapter, the results for the simulations are presented. The results are divided into validation results and results for droplet modelling. The research questions 3 and 4 are answered with the simulation results of this thesis work. In Chapter 6, the conclusions to this work are presented.

2. WIND POWER AND RAIN INDUCED EROSION

The main purpose of this work is to produce droplet impingement simulations on wind turbine blades, and to achieve this, some background information is needed. This chapter starts in Section 2.1 with the concept of wind energy. After that, in Section 2.2 the characteristics of air flowing around the blades are discussed. In Section 2.3, the forces, and moments, which a wind turbine blade experiences when air flows around the blade, are discussed. In Section 2.4 the erosion of the blades and the characteristics of rain droplets are discussed.

2.1 Concept of wind energy

Wind turbines are used for extracting kinetic energy from the wind and converting it to mechanical energy. When examining the stream tube of flow that passes through the cross-sectional area of a wind turbine, the flow slows down as kinetic energy is extracted, and the cross-sectional area of the stream tube increases. This is illustrated in Figure 1.

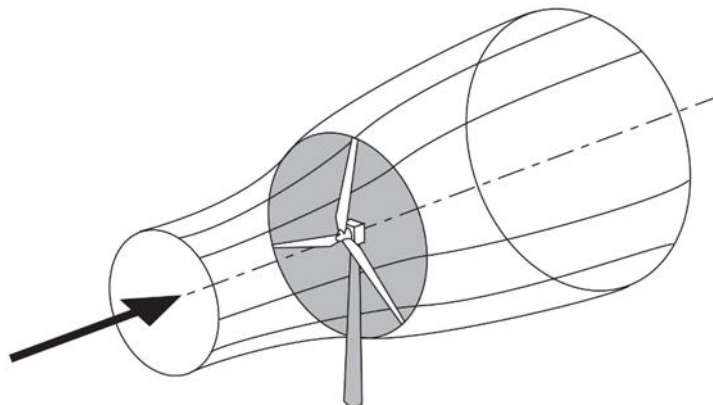


Figure 1. Stream tube concept. [5]

The airflow slows down as it approaches the rotor turbine so that the velocity at the turbine is already lower than the upstream velocity. As the flow velocity decreases before the disc and no work has been done, the static pressure rises. After the rotor, the pressure drops. Far after the rotor the pressure returns to atmospheric pressure, but the velocity remains lower. The flow after the rotor where the pressure and the velocity are decreased, is called the wake. [5]

When examining the energy extraction from the wind, the actuator disc concept is a helpful tool since it allows examining the energy extraction process without any specific turbine geometry. The actuator disc concept is illustrated in Figure 2.

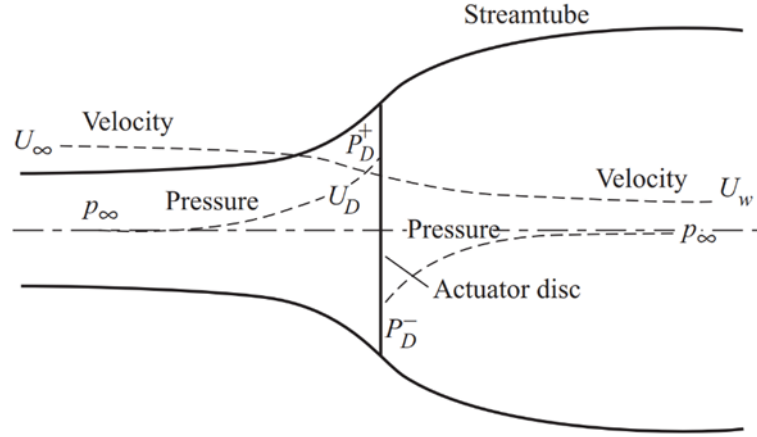


Figure 2. Actuator disc concept. [5]

The pressure rises gradually before the disc, and it is at the highest point right before the disc. Right after the disc pressure drops instantly and then again rises gradually. The velocity does not drop in a single step like the pressure. As the velocity of the flow decreases, the stream tube widens. This is because of the continuity of the fluid flows, which states that the mass flow rate on the stream tube must be equal in all parts of the stream tube. The mass flow can be written as

$$\rho U_{\infty} A_{\infty} = \rho U_d A_d = \rho U_w A_w, \quad (1)$$

where the ρ (kg/m^3) is the density of air, A (m^2) is the cross-sectional area and U (m/s) is flow velocity. [5] Indexes ∞ , d and w refer to conditions in upstream, at the disc and far in the wake. The so-called axial induction factor a (-) represents the decrease of the velocity which the disc induces to the flow. The axial velocity at the disc a can be written with the axial induction factor as

$$U_d = U_{\infty}(1 - a), \quad (2)$$

[5] and rotor thrust can be written with axial induction factor as

$$T_r = \frac{1}{2} \rho A U_{\infty}^2 4a(1 - a). \quad (3)$$

[6] Power of the rotor can be expressed as a product of thrust and the wind velocity at the disc. By combining the Eq. (2) and Eq. (3) power extracted from the wind can be written as

$$P = \frac{1}{2} \rho A U_{\infty}^2 4a(1 - a)^2. \quad (4)$$

[6] A German aerodynamicist Albert Betz derived the maximum power coefficient for actuator disc, and it is known as Betz's law. The detailed derivation of Betz' law can be found for example in Ref. [5]. The value for the maximum power coefficient is 0.593, and

it is achieved when axial induction factor $a = 1/3$ [6]. Power coefficient represents the fraction of power extracted from the wind compared with the available power in the wind.

2.2 Characteristics of airflow around wind turbines

When simulating the airflow over a wind turbine blade, the properties of air in wind turbine operation conditions must be known to get reasonable results. It is not possible to simulate the airflow exactly, therefore some assumptions are needed. In this chapter, the properties of air flow over a wind turbine blade and assumptions made are discussed.

The assumption of continuum flow can be made in the operating conditions of wind turbines, meaning that the motion of individual air molecules is ignored. In continuum flow the collisions of air molecules to the blade are frequent, and the blade sees the air as continuous substance [7].

Air flow can be considered inviscid if there is no friction, thermal conduction, or diffusion. In real life inviscid flows do not exist but some flows can be considered inviscid since viscous effects are small. However, in some flows viscous effects are dominant and can't be ignored. These types of flows are for example flows over airfoils with the high angles of attack. In these situations, the flow detaches from the airfoil and drag forces are high. In viscous flow, when air flows over an airfoil, the flow velocity on the surface of airfoil is zero because of the friction. This is a so called no-slip condition. The flow gradually increases from zero to the surrounding velocity. The flow regime where the flow velocity increases to the velocity of surrounding flow is called the boundary layer. In most regimes of the flow, the shear stress has insignificant impact on the flow. In the boundary layer, the friction forces are dominant, and have great impact on the flow. For incompressible flow boundary layer thickness can be approximated as

$$\delta = \frac{0.37x}{Re_x^{1/5}}, \quad (5)$$

where x (m) is the distance on airfoil and Re_x (-) is local the Reynolds' number. The Boundary layer has a great impact on aerodynamic characteristics of an airfoil. [7] Boundary layer thickness is also an important parameter when defining calculation grids for aerodynamic simulations.

Air flow over a wind turbine blade can often be assumed incompressible. The assumption of incompressible flow simplifies the solution of the flow field around the blade. This assumption can be made if the Mach number is below 0.3. Mach number is the relation of the flow speed and the speed of sound. For perfect gases, the speed of sound can be written as

$$a_s = \sqrt{\gamma R_u T}, \quad (6)$$

where R_u ($\text{J K}^{-1} \text{mol}^{-1}$) is the gas constant, γ (-) is the specific heat ratio and T (K) is the temperature of the fluid [8].

When examining a point on an airfoil surface which directly faces the airflow, and where the streamlines of the flow separate, the velocity is zero. This is called a stagnation point, and it is illustrated in Figure 3.

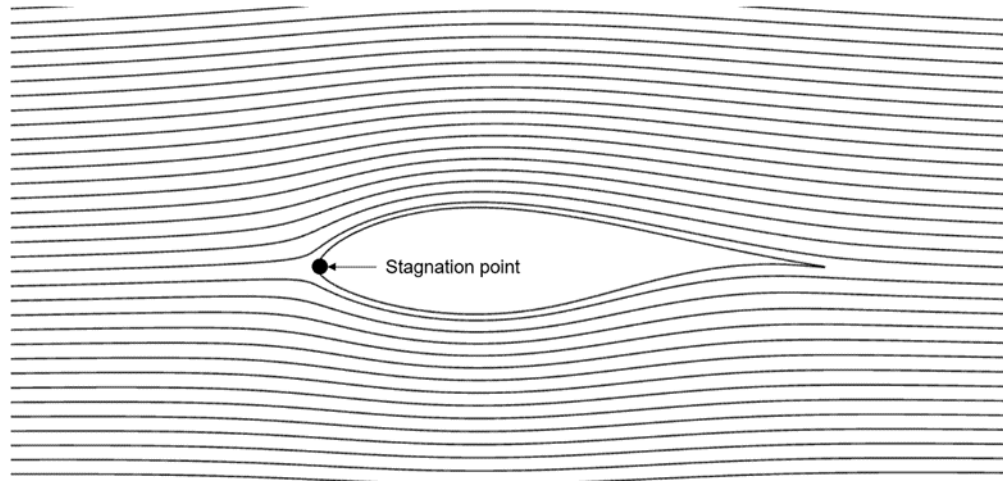


Figure 3. Stagnation point and streamlines of airflow over airfoil.

For a wind turbine blade, the stagnation point is on the leading edge. At stagnation point, the highest pressure of the flow is achieved. If the flow is assumed to be isentropic and adiabatic, and air is assumed as perfect gas pressure ratio can be written as

$$\frac{p_0}{p} = \left[1 + \frac{1}{2}(\gamma - 1)Ma^2 \right]^{\gamma/(\gamma-1)}, \quad (7)$$

Where Ma (-) is Mach number, p_0 (Pa) is stagnation pressure [7]. Similarly, perfect gas temperature ratio can be written for isentropic flows

$$\frac{T_0}{T} = 1 + \frac{\gamma-1}{2}Ma^2, \quad (8)$$

where T_0 (K) is the stagnation temperature and T is the temperature. It is reasonable to assume air as a perfect gas in flows where there are no significant temperature changes [7].

2.3 Forces and moments acting on wind turbine blade

In Chapter 2.1 an actuator disc concept and theoretical maximum power coefficient was discussed. In real life wind turbines have a finite number of blades and a certain geom-

etry. Because of the finite number of the blades, the rotation of the blades and aerodynamic drag, the Betz' limit can't be achieved [6]. In this chapter terminology for wind turbine geometry, and forces and moments acting on a blade are discussed.

A modern-day wind turbine is three bladed and has a horizontal axis. A wind turbine can be considered an upwind turbine if the rotor is facing the wind. Meaning that the tower and nacelle of the turbine are behind the rotor in the direction of the wind. A downwind turbine would be the opposite of this. Most of the wind turbines are upwind [5].

The best power output is obtained when the wind turbine rotor faces directly to the wind. With yaw control wind the turbine rotor can be adjusted in a direction of wind. To get better clearance between the blades and the tower, the blades can be set at a certain angle off the horizontal line. An angle between horizontal line and rotor axis is called the tilt angle. To improve rotor stability the blades can be coned. Cone angle is the angle between the rotor shaft and the blade. In some larger scale wind turbines, the blade pitch can be adjusted to a desired angle. A blade pitch angle is the angle between the plane of rotation and the chord line of the blade. With twisted blades, the local pitch angle depends on the span wise position on the wing. [9]

When airflow hits wind turbine blades, it creates torque that rotates the rotor blades. Since every force has a counter force, the blades create equal and opposite direction force to the airflow. As a result of this, the flow in the wake has velocity component tangential to the blade rotation. Tangential induction factor a' represents the tangential velocity blades induce to the flow. Blade rotating with an angular velocity of Ω induces a tangential velocity of $2\Omega ra'$ right after the blade. [5]

One very important parameter in wind turbine design is a tip speed. A tip speed ratio is the ratio between blade tip speed and wind speed, and it can be written as

$$\lambda = \frac{u_t}{U_\infty}, \quad (9)$$

where u_t (m/s) is the tip speed of the blade tip [9]. Speed ratio can also be determined at any radial point of the blade by substituting the tip speed with local speed. This ratio is called a local speed ratio. The power coefficient is generally plotted as a function of a tip speed ratio. This is a so-called performance curve. In Figure 4, a typical performance curve is shown.

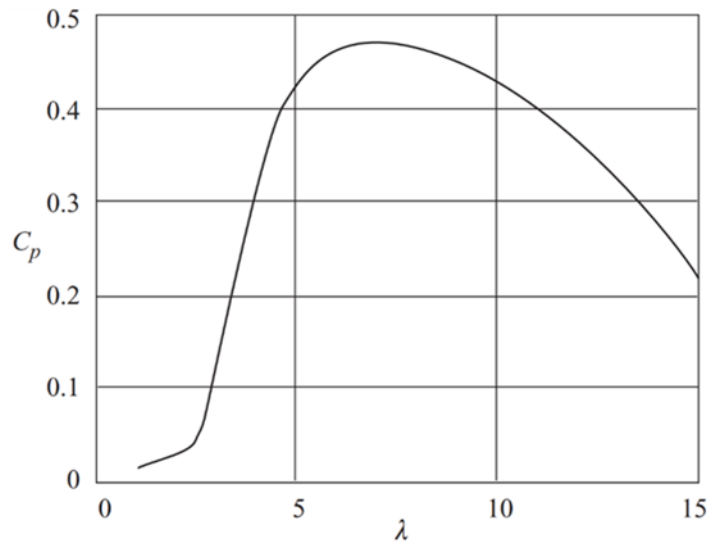


Figure 4. Performance curve. [5]

The maximum power coefficient is obtained when the axial induction factor $a = 1/3$. At low tip speed ratios, the axial induction factor can be significantly lower than $1/3$, and angles of attack high leading to stalled conditions. At higher tip speed ratios, the axial induction factor is high and angles of attack low, which leads to high drag. To get the best power output it would be desirable that the wind turbine could operate with a constant tip speed ratio. [5]

Different wind turbine blades have a specific geometry and can have a different cross-sectional shape. In Figure 5, an airfoil geometry is presented.

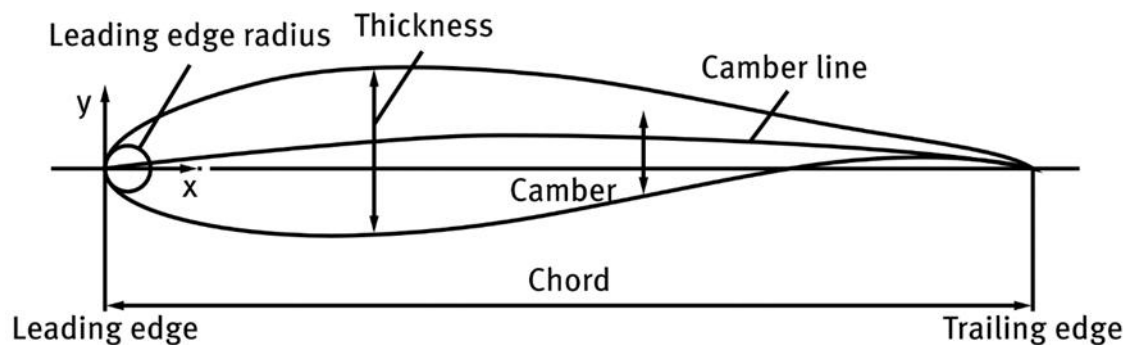


Figure 5. Airfoil geometry. [10]

In Figure 5, camber line is the mean line between the surfaces of airfoil. Chord is the distance between leading edge and trailing edge. Thickness is the maximum distance between upper and lower surface of an airfoil.

All the forces and moments acting on the blade are due to pressure distribution and shear stress over a blade. Pressure acts normal to the surface of blade, and shear stress acts tangential to the surface. The air flows faster on the upper surface of airfoil, resulting

in lower net pressure than on the lower side of the airfoil. The upper side of the airfoil is called a suction side, and lower side a pressure side. The aerodynamic force and moment acting on the blade are the net result of pressure and shear stress integrated over the blade. [8] In Figure 6, aerodynamic forces of an airfoil are presented.

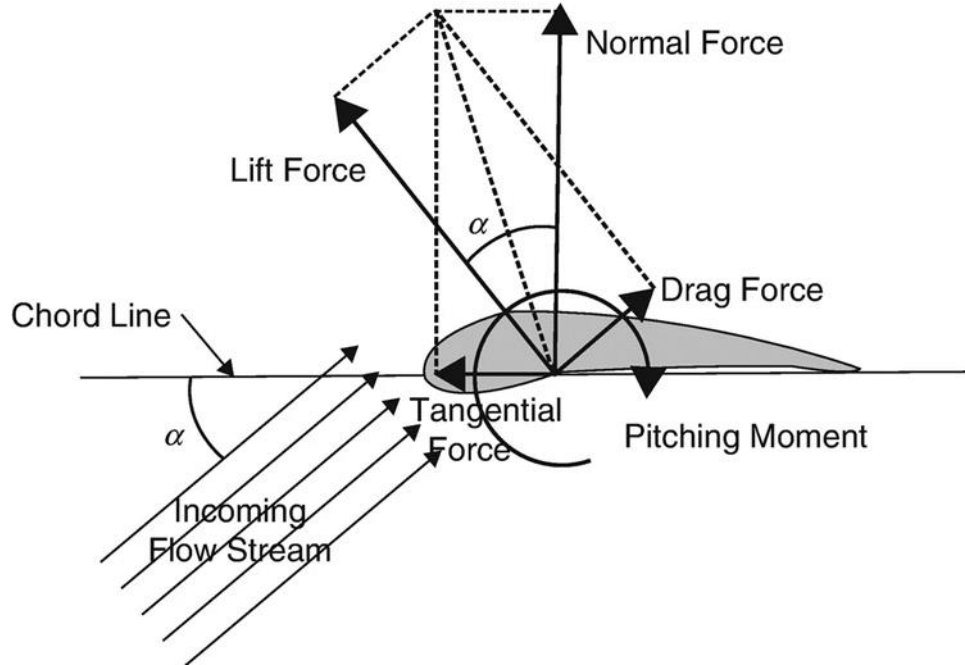


Figure 6. Forces acting on an airfoil. [11]

In Figure 6, chord line is a straight line from leading edge to trailing edge and α angle of an attack is the angle between chord and freestream velocity. Normal force is perpendicular to the chord line, and tangential force is parallel to the chord line. Aerodynamic lift L is perpendicular to the freestream velocity, and drag D is parallel to the freestream velocity. When the angle of an attack is increased, the lift increases until the point where the flow separates from the wing, and it is called a stall [8].

The aerodynamic force will be the same at any point of the airfoil, but the moment depends on where the force is applied. The center of pressure is a point on the airfoil where aerodynamic moment is zero. The aerodynamic center of an airfoil is the point where moment stays constant when the angle of attack changes. On most low-speed airfoils aerodynamic center is at 25 % chord length. [8]

Dimensionless coefficients of aerodynamic forces and moments are often used instead of absolute values. For example, lift and drag coefficients for an airfoil can be calculated as follows

$$C_l = \frac{L}{q_\infty S}, \quad (10)$$

$$C_d = \frac{D}{q_\infty S}, \quad (11)$$

where S (m^2) is a reference area and q_∞ (Pa) is freestream dynamic pressure. It is a general custom to mark two-dimensional coefficients with a lowercase subscript, and three-dimensional coefficients with an uppercase subscript. The dynamic pressure can be written as

$$q_\infty = \frac{1}{2} \rho_\infty U_\infty^2, \quad (12)$$

where ρ_∞ and U_∞ are the free stream density and velocity. The dynamic pressure can be also expressed with the Mach number as

$$q_\infty = \frac{\gamma}{2} p_\infty Ma_\infty^2, \quad (13)$$

where γ is the ratio of specific heats and Ma_∞ is the Mach number of the flow. The power coefficient for a wind turbine can be written with a help of tip speed ratio as

$$C_P = C_Q \lambda, \quad (14)$$

where C_Q is torque coefficient, which can be written as

$$C_Q = \frac{Q}{\frac{1}{2} \rho U_\infty^2 A R}, \quad (15)$$

where A is the rotor swept area and R (m) is the radius of the rotor. The rotor thrust coefficient can be written as

$$C_T = \frac{T_r}{q_\infty A}, \quad (16)$$

where T_r is the thrust of the rotor. The coefficient forms of forces allow the comparison between different rotors and airfoil shapes. [8]

2.4 Rain droplet impingement and blade erosion

Wind turbines have grown in the last decades, especially offshore wind turbines. Placing wind turbines offshore can be appealing since the tip speeds are not limited there due to noise restrictions, and wind conditions are typically good offshore. However, construction and maintenance costs are typically higher in offshore wind turbines. A large-scale offshore wind turbine can have a tip speed of 100 m/s. With higher tip speeds, the impact velocities of rain droplets impinging the wind turbine blades also increases. [2]

The erosion of the blades takes place first on the leading edge close to the tip, where the velocities are the highest. Effects of it can be seen in a couple of years after the installation of a new turbine [12]. The effects off erosion to the annual energy production

of a wind turbine has been studied by Sareen et al. [4]. Erosion has an impact on the aerodynamic properties of the blade by increasing the aerodynamic drag and decreasing the lift. Therefore, erosion affects the overall efficiency of the wind turbine. It was estimated that depending on the severity of the erosion, the loss in annual energy production can be as high as 25 %. There are ways of protecting the blades. For example, the opportunity of lowering the tip speed of the turbine during heavy rains has been studied by Bech et al. [13]. It was concluded that the loss of energy production due the lower tip speed wouldn't exceed the loss of energy production due to erosion. A comprehensive review of existing leading edge protection systems, like coatings and protective tapes, can be found in Ref. [2].

When examining rain induced erosion, it is important to understand characteristics of rain. Rain droplets have a size distribution that depends on the intensity of the rain. Different size droplets have a different terminal velocity. The most common way of describing droplet size distribution is the method developed by Best. In Figure 7, a probability density of droplet diameters is plotted with different rain intensities.

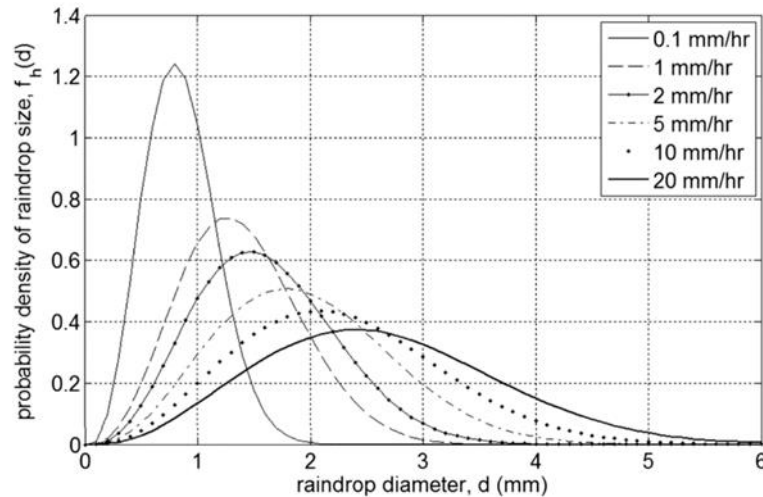


Figure 7. Rain droplet diameter probability density with different rain intensities. [14]

The size distribution of rain droplets depends on the intensity of the rain. With the light intensity of rain, the droplet diameter of below 1 mm is the most common, and with the heavy rain of 20 mm/hr the droplet diameter of approximately 2.5 mm is the most common. As the droplet radius grows over 6 mm, they tend to split into separate droplets [13]. The terminal velocity of the droplets increases as the mass of the droplets increase. In Figure 8, terminal velocity is plotted as a function of droplet diameter.

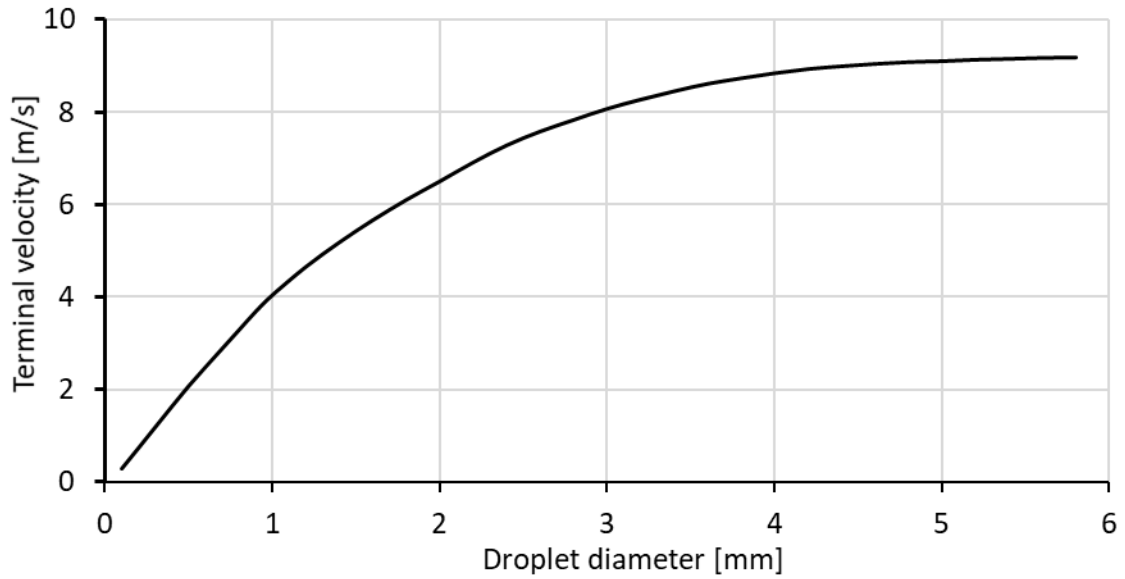


Figure 8. Droplet terminal velocity as a function of droplet diameter. Data from Ref. [15]

Leading edge erosion depends on the velocity of the blade and characteristics of the rain. The characteristic of rain depends on the geographical location, for example the characteristic of rain is different in offshore conditions than in onshore conditions. Rain droplet diameters and intensity probabilities have been studied for offshore conditions in Europe by [12]. In this study, the rain was categorized into four categories based on the intensity of the rain. It was suggested that since the heaviest rains with bigger droplet sizes were quite rare, and since the erosion of the blade can happen within a couple of years of the turbine lifecycle, the lighter intensity rain can also induce erosion.

The velocity of a droplet approaching a wind turbine consists of wind speed and terminal velocity components. The droplet velocity relative to the ground can be expressed as

$$W_g = \sqrt{U_\infty^2 + \gamma_d^2}, \quad (17)$$

where U_∞ is the wind velocity and γ_d (m/s) is the terminal speed of the droplet. As the droplet gets closer to the rotor, the trajectory of the droplets gets affected by the flow field induced by the rotor. When the particle distance from the rotor is about the size of rotor diameter, the particle velocity relative to the blade can be expressed as

$$W_b = \sqrt{U_\infty^2(1-a)^2 + (\Omega r - \gamma_d \sin\psi)^2}, \quad (18)$$

where Ω (rad/s) is the rotational speed of the rotor, r is the radius of the blade and ψ ($^\circ$) is the blade azimuth angle. Trajectories of rain droplets colliding with a wind turbine blade depend on the inertia of the droplets, and aerodynamic drag of the droplets. If inertia of the droplet is high compared with drag, the droplet trajectory will not get affected by the air flow as easily. [16]

3. SIMULATION OF AIRFLOW AND WATER DROPLET IMPINGEMENT

There are different numerical methods for predicting aerodynamic forces and moments of wind turbines. Methods based on blade element momentum theory (BEM) have been widely used for decades in wind turbine industry. BEM is relatively accurate and simple method for predicting the loads of wind turbines, but disadvantage is that it relies on experimental data, which is not always attainable. In CFD methods, no experimental data is needed but computational cost of the simulations is higher compared with BEM. CFD has become more and more important tool for predicting wind turbine aerodynamic as the computational power of computers has gone up in last decades.

As computers have become more powerful, CFD methods for predicting forces and moments acting on a wind turbine blades have become more useful. Valuable information can be obtained with more time- and cost-efficient way compared with experimental results. Proper understanding about the numerical methods and models is important. Choosing the right parameters for calculating the flow over a blade can be crucial for the accuracy of the results. In this chapter numerical methods for modelling the aerodynamics of wind turbines are discussed. The governing equations related to the fluid flow, turbulence models, modelling the rotation of blades and particle impingement are discussed. This chapter aims to answer the second research question.

3.1 Governing equations for airflow around wind turbines

The motion of fluids can be described with partial differential equations. To solve partial differential equations boundary conditions are needed, and fluid needs to be assumed continuum meaning that the molecular motion of the fluid can be ignored [17]. The partial differential equations governing the fluid flow are called Navier Stokes equations. There is no analytical solution for Navier Stokes equations, and numerical methods are needed to solve them. They are based on the conservation of mass, momentum, and energy. Navier Stokes equations can be presented in various forms, for example in vector form or integral form. It depends on the application which of the forms is most suitable. All the governing equations can be written in the form of general transport equation

$$\frac{\partial(\rho\phi)}{\partial t} + \nabla \cdot (\rho\phi u) = \nabla \cdot (\Gamma \nabla \phi) + S_\phi. \quad (19)$$

Equation (20) is a general transport equation for variable ϕ . The first term on the left side states the rate of change of variable ϕ , and second term is a convection term. On the

right side of equation first is diffusion term where Γ is the diffusion coefficient and S_ϕ is source term for variable ϕ [17].

The first equation is called a continuity equation, and it describes the conservation of mass. It can be written as

$$\frac{\partial \rho}{\partial t} + \nabla \cdot (\rho \mathbf{u}) = 0, \quad (20)$$

where ρ is density of the fluid, t is time and \mathbf{u} is the velocity containing direction components [17]. The first term on the left describes the change in density over time, and the second term is a convection term which describes the net mass flow in and out of the control volume. So, in physical sense the continuity equations states that mass can't be created or destroyed. For Mach numbers under 0.3, the flow can be assumed as incompressible and the density constant so the first term in Eq. (20) becomes zero [8].

The second governing equations is momentum equation which is based on the Newtons second law, and it states that the force is equal to the change of momentum over time. The force acting on the fluid can be divided into body forces such as gravity, and surface forces such as pressure and viscous forces. The momentum equation for x component can be written as

$$\frac{\partial(\rho u)}{\partial t} + \nabla \cdot (\rho u \mathbf{u}) = -\frac{\partial p}{\partial x} + \nabla \cdot (\mu \nabla u) + S_{Mx}, \quad (21)$$

where p is pressure, μ is dynamic viscosity and S_{Mx} is a source term, which represents the body forces. In a similar way the momentum equation can be written in two other directions, and they can be found in Ref. [17]. In physical, sense the momentum equation states that the sum of change in momentum over time and place is equal to the sum of forces. First term on the right side is the pressure force, and second term is friction forces. Last term on the right side stands for source terms (for example gravity).

The third equation is energy equation, and it is based on Newtons first law. The sum of net heat added to a fluid particle, and the net work done by the particle is equal to the increase in the energy of the particle. The energy equation can be written with internal energy as

$$\frac{\partial(\rho i)}{\partial t} + \nabla \cdot (\rho u \mathbf{i}) = -p \nabla \cdot \mathbf{u} + \nabla \cdot (K \nabla T) + \Phi + S_i, \quad (22)$$

where i is the internal energy, K is the heat conduction, T is the temperature and Φ is a dissipation function including friction forces [17]. First term on the right side is work done by pressure, and the second term is the net heat rate added to fluid by heat conduction. Last term on the right side is the source term.

Above mentioned governing partial differential equations needs to be discretized so that the numerical solution can be obtained. Before discretized forms of governing equations can be obtained, a method for solving the pressure field of the flow must be figured, since there is no transport equation for pressure, but it is in governing equations. For compressible flows, continuity equation can be used as transport equations for density, and energy equation as transport equation for the temperature, and pressure can be obtained from the equation of state. For incompressible flow density is constant, and pressure can't be solved similarly as in compressible flow. In this case, to solve the flow field, coupling between pressure and velocity is needed.

There are several iterative algorithms to solve pressure velocity linkage. One of these is a SIMPLE (Semi-Implicit Method for Pressure Linked Equations) algorithm that uses guessed velocity components to solve pressure and velocity fields from momentum equations. Then continuity equation is used to deduce a pressure correction equation, which is used to update pressure and velocity fields. Since SIMPLE algorithm was developed, updated versions of it have been invented like SIMPLER (SIMPLE Revised), and SIMPLEC (SIMPLE-Consistent) algorithms. In SIMPLER, a discretized equation for pressure is derived for pressure from continuity equation instead of correction equation. In SIMPLEC the velocity correction terms are improved in comparison with the standard SIMPLE algorithm. More information about pressure velocity coupling can be found in Ref. [17].

The most common way of solving fluid flow problems is a so-called Finite volume method (FVM) also known as a control volume method. In FVM the flow domain is divided into a finite number of cells, and flow properties are solved individually in every cell. Other numerical methods are Finite Difference Method and Finite element Method.

In FVM, Eq. (19) is integrated over a control volume (one cell). The convection term and the diffusion term are converted into a surface integral with Gauss's divergence theorem. With this, the fluid properties in the control volume and on the surfaces of the control volume can be calculated. The number of cells in the domain is closely related to the accuracy of the solution. In wind turbine simulations especially the number and size of the cells adjacent to the blade is critical to model boundary layer effects properly. To help determine the first cell height adjacent to wall, dimensionless distance y^+ can be used. The dimensionless distance is defined as

$$y^+ = \frac{yu_f}{\nu}, \quad (23)$$

where y is absolute value of the distance from the wall, u_f is friction velocity and ν is kinematic viscosity [17]. When designing calculation grids, the first cell height is usually designed so that $y^+ = 1$ to ensure that the first cell is in the viscous boundary layer.

3.2 Modelling turbulence

In nature wind is always turbulent. Turbulence is always three-dimensional and chaotic. The smallest scales of turbulence are so called Kolmogorov microscales. To model turbulence accurately, the cell size and the time step would have to be smaller than these microscales. This would lead to computationally demanding simulations. In large scale fluid flow problems, it is often enough to simulate the mean flow. However, the effects of turbulence on the mean flow can't be ignored. To model turbulence effects on the mean flow, above mentioned Navier Stokes equations can be time averaged.

Reynolds Averaged Navier Stokes (RANS) modelling is a very common way of simulating practical fluid flow problems. In RANS, the variables in Navier Stokes equations are divided into a time averaged and a fluctuating component. This leads to new variables in governing equations, and to solve them turbulence models are needed. Other simulation methods are Large Eddy Simulation (LES) and Direct Numerical Simulation (DNS). In DNS the flow field and turbulence are solved precisely. This means that the time step and the cell size needs to be smaller than the Kolmogorov scales. This is computationally demanding, and no industrial size problems can be simulated using DNS. LES modelling is intermediate of DNS and RANS simulations, in which the larger scale turbulence is modelled accurately, and smaller scale is approximated with turbulence models. More information about numerical methods can be found in Ref. [17].

By the result of time averaging the governing Navier Stokes equations, new variables appear in the momentum equation. In total six new stress terms are added: three normal stresses and three shear stresses [17]. These are called Reynolds Stresses. To solve these Reynolds stresses, turbulence models are used.

There are several turbulence models available and choosing the suitable option for the specific case is important. There is no general turbulence model that is suitable for all flow simulations. The models can vary in complexity and accuracy. One of the most common turbulence models are the 2-equation models $k - \varepsilon$ and $k - \omega$. In these models, The Reynolds stresses are calculated with two additional equations. In $k - \varepsilon$ model turbulent kinetic energy k and its dissipation rate are ε solved with separate partial differential equations to calculate the Reynolds stresses. In $k - \varepsilon$ the turbulent viscosity is assumed to be isotropic, which may lead to inaccurate results in complex flows.

In $k - \omega$ the turbulent kinetic energy is calculated similarly to the $k - \varepsilon$ model but the turbulent dissipation rate is replaced with turbulent frequency $\omega = \varepsilon/k$. A hybrid model of these two models is SST (Shear Stress Transport) $k - \omega$. In this model the turbulence is modelled with $k - \varepsilon$ in the freestream region of the flow, and with $k - \omega$ in the near wall regions. The transport equation for turbulent kinetic energy k in SST $k - \omega$ model is

$$\frac{\partial}{\partial t}(\rho k) + \frac{\partial}{\partial x_i}(\rho k u_i) = \frac{\partial}{\partial x_j} \left(\Gamma_k \frac{\partial k}{\partial x_j} \right) + G_k - Y_k + S_k + G_b, \quad (24)$$

and transport equation for turbulent dissipation rate ω is

$$\frac{\partial}{\partial t}(\rho \omega) + \frac{\partial}{\partial x_i}(\rho \omega u_i) = \frac{\partial}{\partial x_j} \left(\Gamma_\omega \frac{\partial \omega}{\partial x_j} \right) + G_\omega - Y_\omega + S_\omega + G_{\omega b}. \quad (25)$$

In these equations, G_k is the generation term for turbulent kinetic energy, G_ω is generation term for ω , Γ is effective diffusivity term, Y is dissipation term, D_ω is a cross-diffusion term, S is source term, G_b and $G_{\omega b}$ are buoyancy terms [18]. In this model, the boundary layer effects can be simulated more accurately while still being accurate in the free stream region of the flow. For this reason, SST $k - \omega$ is a suitable model for simulating flows over airfoils, where the boundary layer effects are important.

Another variation of SST $k - \omega$ is the transition model where two more transport equations are added to the SST $k - \omega$ model transport equations mentioned above. The added transport equations are for intermittency and for transition onset criteria. With this turbulence model the transition of laminar to turbulent can be modelled but it highly relies on empirical correlation terms [18].

There is also a turbulence model that solves the Reynolds stresses. In this RSM model seven additional equations are needed: six for the Reynolds stresses and one for the turbulent dissipation rate. The RSM model adds computational cost without any significant increase in accuracy in some cases. RSM is the most suitable being used when there are high swirl or rotational velocities [18].

Villalpando et al. [19] have studied turbulence models for steady state 2D flows over airfoil. In this study CFD model of flow over NACA 63-415 airfoil was compared with experimental results. Turbulence models compared were one equation Spalart-Allmaras model, two equation SST $k - \omega$ and $k - \varepsilon$ model and seven equation RSM model. The SST $k - \omega$ gave the most accurate results. Whereas, RSM model was found to add computational cost of the simulation without any significant improvement to the results.

The NREL phase VI rotor, also used in the validation of simulation results in this work, has been studied by Ji et al. [20] and Sagol et al. [21]. In these studies, the effects of

different turbulence models to the accuracy of the results were studied. Sagol et al. compared two equation models and concluded that with SST $k - \omega$ model, the results of pressure coefficient, shaft torque and bending moment were most in line with the experimental results. Ji et al. used SST $k - \omega$ and transition SST turbulence models. It was concluded that with low wind speeds both models give results that are in good agreement with experimental results. As wind speed is increased, both models start to have some deviation from experimental value due to incapability to model the flow separation from the blade with a steady state solver.

With the above-mentioned studies, it can be concluded that SST $k - \omega$ and transition SST are suitable turbulence models for wind turbine simulations. Both can quite accurately model turbulence without excessively adding computational cost. However, both models are inaccurate when there is high flow separation from the blade.

3.3 Simulating rotation of the wind turbine blades

When CFD simulation includes moving parts, it often requires the simulation to be transient. It is possible to model moving parts as a steady state by using a moving reference frame. For example, a rotating wind turbine blade can be simulated as a steady state with this method, but the rotational velocity must be constant. In a moving reference frame simulation, there are additional terms in the momentum equations so that the acceleration of the fluid can be solved. In ANSYS Fluent the momentum equations can be expressed using either relative velocities or absolute velocities [18]. The absolute velocity formulation should be used in case where the rotating component is small in comparison with the entire calculation domain. For example, if a relatively small blade is placed in a large calculation domain, absolute velocity formulation should be used.

The entire calculation domain can be referred as single reference frame or multiple reference frames can be used. In the simulation of wind turbines with multiple blades it is common to take advantage of symmetry, and model only one of the blades to save computational power. In Figure 9, a calculation domain for a wind turbine blade is illustrated in a rotational reference frame.

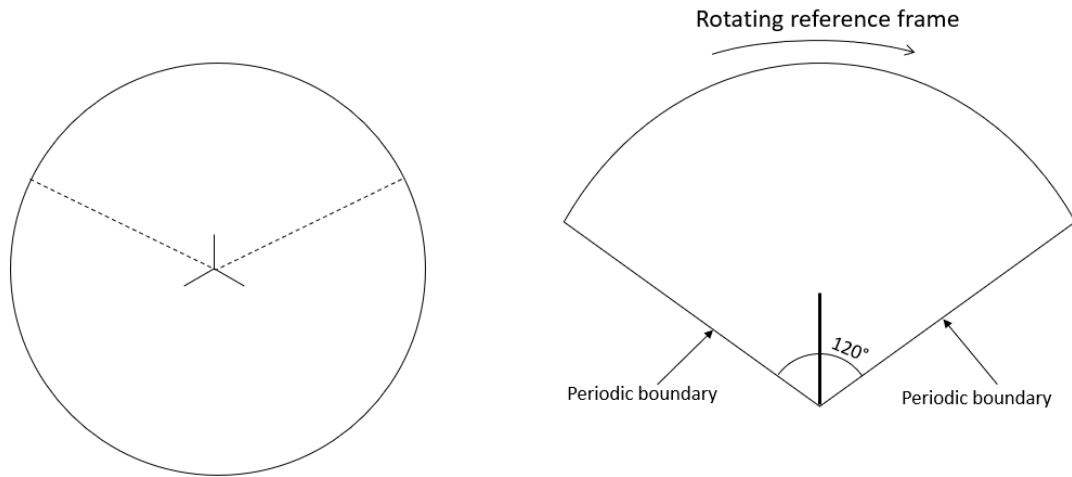


Figure 9. Rotating reference frame with periodic boundaries. Adapted from Ref. [18]

If the calculation domain is relatively simple, the entire domain can be referred as a single moving reference frame. On the left of Figure 9, a complete three bladed rotor is in the middle of the calculation domain, and on the right side is a calculation domain for one blade with periodic boundaries. The advantage of modelling only one of the blades is that computational cost is saved. The boundaries of the calculation domain must be periodic to the axis of rotation [18]. Simulating wind turbine blades with rotating reference frame and periodic boundaries is a common method [22–25].

The boundaries of the calculation domain need to extend far enough upstream and downstream from the blade to capture the effect of the wake. Since the stream tube of airflow also widens, the height of the domain needs to extend far enough. NREL Phase VI rotor has been studied with CFD methods by multiple studies [20–27]. In these studies, the cylindrical domain size was used with periodic boundaries. The domain boundaries were set 2-5 times the radius of the blade upstream and 4-8 times the radius of the blade downstream. The cylindrical far field had a radius of 3-5 times the radius of the blade.

3.4 Simulating water droplets in airflow

To simulate droplet trajectories and impact speeds on a wind turbine blade, a discrete phase model (DPM) available in ANSYS Fluent can be used. It uses Lagrangian particle tracking to calculate the trajectories of the discrete phase droplets in the main phase. Since the volume fraction of droplets is low in comparison with the main flow, the interactions between droplets can be ignored. With DPM model a one-way or two-way coupling method can be used. In two-way coupling the discrete phase droplets have an effect on the air flow. With the one-way coupling the droplets have no impact on the flow field of the main phase. With one-way coupling the particle trajectories can be calculated

in the post processing of the converged air flow solution, which makes calculating large quantities of droplets faster [18]. The droplets are released in the flow field with a specific release point and a velocity. In Figure 10, two particle trajectories in a 2D domain are calculated with DPM model.

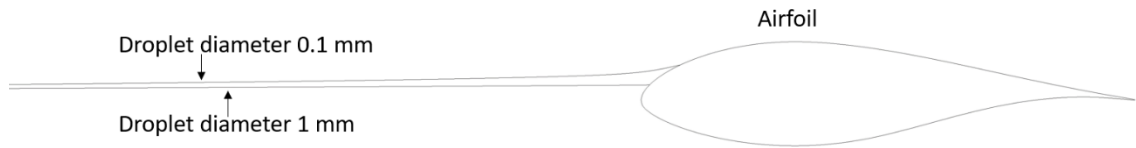


Figure 10. Particle trajectory in 2D domain.

In Figure 10, particles with the diameters of 1 mm and 0.1 mm are tracked in a 2D calculation domain. Particles are tracked with the one-way coupling method, and they are released from the same position upstream, and the same initial velocity (release point far upstream and not visible in Figure 10). The particle with a smaller diameter adapts the continuous phase faster than the bigger particle, therefore the impact position is different.

Particle tracking works in similar manner in 3D simulations as in 2D, but a moving reference frame and periodic boundaries add complexity to the simulation. In Figure 11, a droplet trajectory in a rotating reference with periodic boundaries is presented.

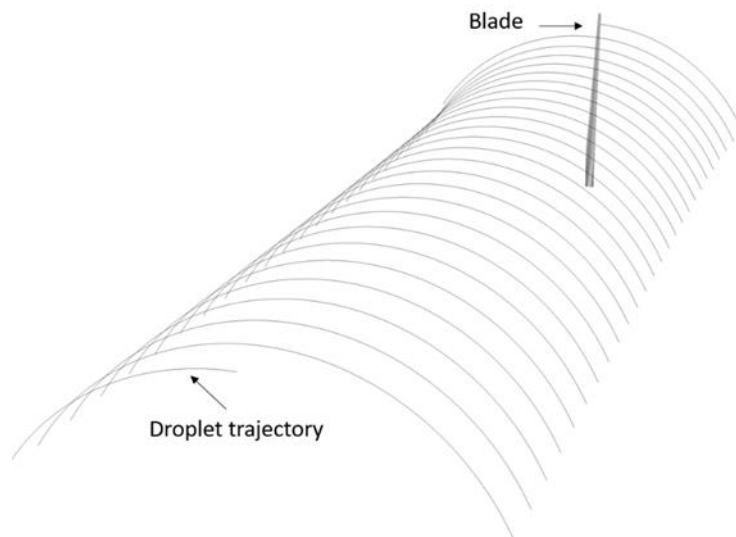


Figure 11. Droplet trajectory in a rotating reference frame with periodic boundaries.

When simulating particle trajectories in a rotating reference frame, it is needed to define if the particle is tracked in a relative or absolute frame of reference. In a case as in Figure 11, the fluid domain is in a rotating motion relative to the stationary blade, and the particle is tracked in a relative frame of reference. In ANSYS Fluent theory guide Ref. [18] it is

said that the accuracy of particle tracking can be increased by dividing the computational cells into subsets, and particles are tracked in these subsets instead of the computational cells. If the particles cross the periodic boundaries, (like in the case of Figure 11) cell subsets can be created by using cell face centroids to avoid discontinuities in the particle tracks when crossing over periodic boundaries.

4. MATERIALS AND METHODS

In this chapter, the methodology for the validation of FFA-W3-211 airfoil and NREL Phase VI presented. Calculation methods for IEA-15-240-RWT and particle tracking methods for both 2D airfoil and 3D blade are presented. All the calculation meshes are made with ANSYS ICEM software using structured meshing. Fluid Flow simulations are made with ANSYS Fluent using a steady state solver.

4.1 Workflow

The purpose of this work is to examine the impact speeds of droplets impinging the surface of a wind turbine blade using CFD tools. To ensure the accuracy of the results, the CFD simulation results for forces and moments acting on a blade are validated by comparing the simulation results with existing wind tunnel test results. After the validation of the simulations, a flow field around the blade of IEA-15-240 RWT is calculated. The droplet simulations are made to this blade. The workflow of this work can be divided into different sections which are presented in Figure 12.

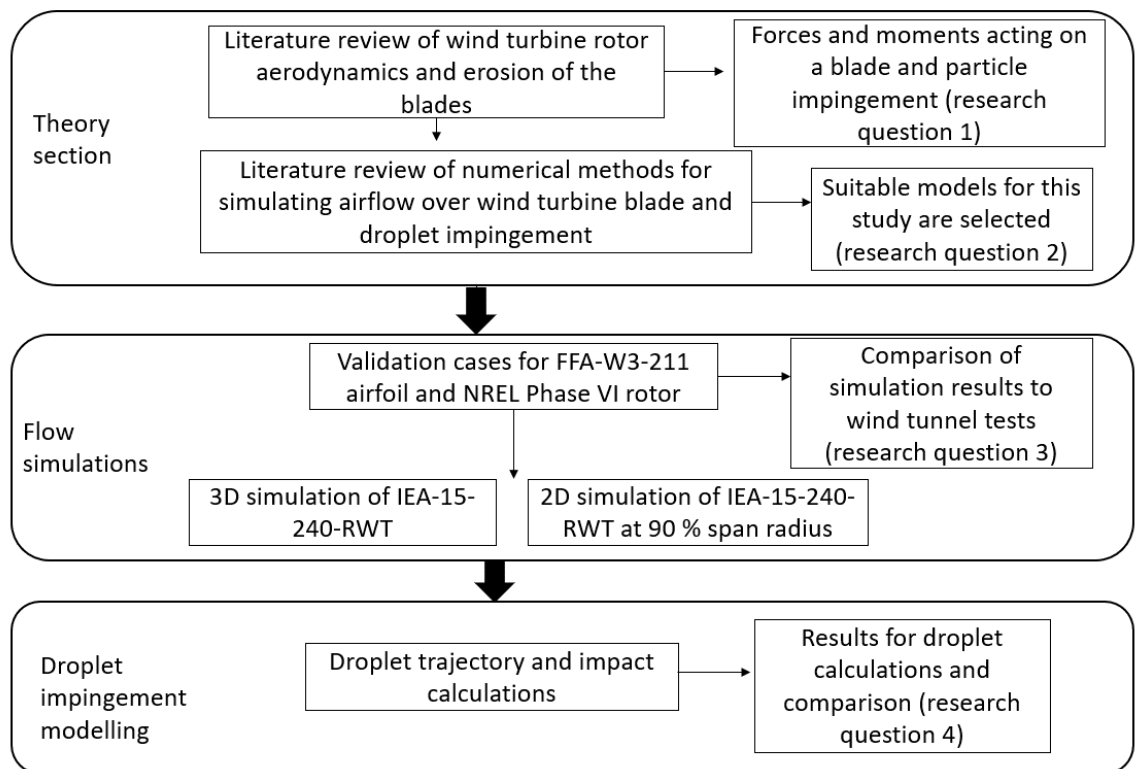


Figure 12. Workflow for the thesis research.

The models used in the validation cases are based on those described in Chapter 3. The results of the flow field of IEA-15-240 RWT are compared with results obtained with

OpenFAST program since no experimental results are available. OpenFAST is an open-source simulation tool for wind turbines developed by National Renewable Energy Laboratory, and it is based on the BEM method [28].

4.2 Validation of 2D and 3D simulations

Validation of FFA-W3-211 airfoil

For the validation of 2D simulations, FFA-W3-211 airfoil with chord length of 1 m was used. The airfoil had a blunt trailing edge with the thickness of 0.00262 m. The experimental wind tunnel test results were obtained from Ref. [29], and the coordinates for airfoil were obtained from Ref. [30]. The results for lift, drag and moment coefficients were compared with the experimental results. Simulations were carried out with five different angles of attack: 0° , 2.5° , 5° , 7.5° and 10° .

Since the trailing edge thickness was not mentioned in Ref. [29], the first task was to make sure that the trailing edge thickness was similar for the airfoil used in experimental results as in Ref. [30]. To verify the trailing edge thickness, the lift, moment, and drag coefficient were calculated with Xfoil software with the same boundary conditions and Reynolds' number as in Ref. [29]. The coefficients calculated in this work matched the Xfoil results in Ref. [29], so it was concluded that the airfoil trailing edge thickness was similar in both references.

ICEM CFD software was used for generating structured mesh around the airfoil. The airfoil was placed in the middle of the fluid domain, and the boundaries were set 20 times chord length away in all directions. The domain and the mesh are shown in Figure 13.

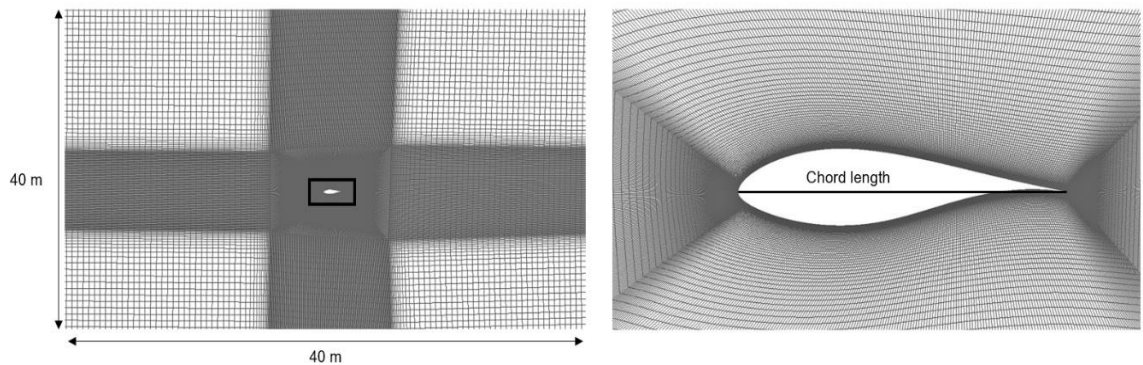


Figure 13. Full calculation domain (left) and close-up view around the airfoil (right).

In Figure 13, the full calculation grid is shown on the left, and a closer view around the airfoil is shown on the right. The chord length is 1 m, so the domain boundaries were set 20 meters away from the airfoil in all directions. The mesh consisted of around 200 000

nodes with thicker cells around the airfoil. The first cell height was calculated with a y^+ calculator with the desired y^+ value of 1. The growth ratio of cell size was set to 1.1. The mesh orthogonal quality, aspect ratio and overall quality was examined. The orthogonal quality was in the range of 0.5-0.6, aspect ratio was in the worst parts over 1000, which is due very thin cells on the airfoil surface, and overall quality of above 0.9. The mesh quality criteria evaluated in this work are based on those used in ANSYS Fluent. More information about the quality criteria can be found in ANSYS Fluent user's guide [31].

The mesh independence study was made with four different mesh sizes (100 000, 200 000, 250 000 and 300 000 nodes) to verify that the results will not depend on the mesh size. The angle of attack 0° was used for mesh independence study. In the mesh independence study only the number of cells was changed, the spacings and first cell height was kept the same.

In the simulation models, energy equations were turned on and $k - \omega$ SST turbulence model was used for its capabilities of modelling near wall turbulence and moderate computational cost as discussed in Section 3.2. The air density was calculated with ideal gas law and the viscosity with Sutherland's law. The Reynolds' number used was 1.8 million and Mach number 0.15. The inlet was set as a pressure inlet and outlet was set as a pressure outlet. Airfoil surface was set as wall with no-slip condition turned on. SIMPLEC pressure-velocity coupling method was used, and the discretization scheme was second order upwind.

The calculation was continued for about 10 000 iterations for each simulation. The results were considered converged after the monitored results reached a constant value, and all the scaled residuals were below 10^{-6} . The monitors were set for the coefficients of lift, drag and moment. The center of moment was set to 25 % of the chord length measured from the tip of a leading edge.

Validation of NREL Phase VI

For 3D simulation validation NREL Phase VI two bladed rotor with 5.029 m radius was used. The results were compared with wind tunnel test results available in Ref. [6]. In the report, several tests were executed. For the validation, four of the tests with different wind speeds were chosen for comparison. The test conditions are shown in Table 1.

Table 1. *Test conditions, information from Ref. [6]*

Test #	1	2	3	4
Average Wind Speed [m/s]	7.0	10.0	13.1	15.1
Average Air Density [kg/m ³]	1.246	1.246	1.227	1.224
Blade Collective Tip Pitch Angle [deg]	3.0	3.0	3.0	3.0
Average Rotor Rotational Speed [rpm]	71.9	72.1	72.1	72.1

Steady state simulation of the wind turbine was made using a moving reference frame with a rotational speed of 71.9 in the first simulation, and 72.1 for the rest of the tests. Wind speeds for the simulations were ranging from 7 m/s to 15.1 m/s. Blade pitch angle was set for 3° measured from the tip chord line for all the four cases.

Structured mesh of 4.8 million cells was generated with ICEM CFD. Blade was placed in the middle of the calculation domain, and O-grid was placed around the blade. Boundaries were set 100 meters away from the blade for both upstream and downstream direction (about 10 diameters of the rotor). A circular far field with a 100 m radius was made. The bottom side of the domain was made with periodic boundaries. Calculation domain boundaries are shown in Figure 14.

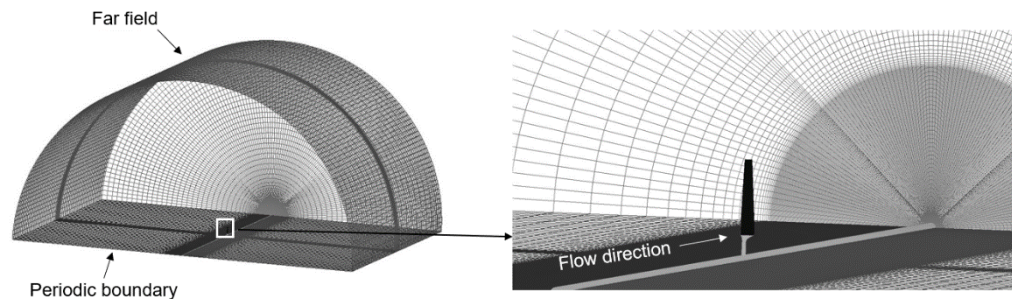


Figure 14. The entire calculation domain (right), and closer view on the blade in the middle of the domain (left).

Again y^+ calculator was used to determine the first cell height adjacent to the blade surface. A Growth factor of 1.2 was used. The surface mesh of the blade was made so that the trailing edge and leading edge had thicker cell count, and a growth factor was set to 1.2. The mesh overall quality was examined. The quality criterion was only about 0.2 at the lowest. Thin trailing edge, and twist of the blade were the reasons of why better quality was not achieved. However, there were only few cells with the lower quality, and it was assumed that it wouldn't affect the convergence of the results.

Calculations were made with four different inlet wind speeds: 7, 10, 13 and 15 m/s, and forces and moments acting on the blade were compared with measured data. The blade

was divided into five span wise sections. The local normal force coefficient and local dynamic pressure was calculated at these locations. Span wise locations are shown in Figure 15.

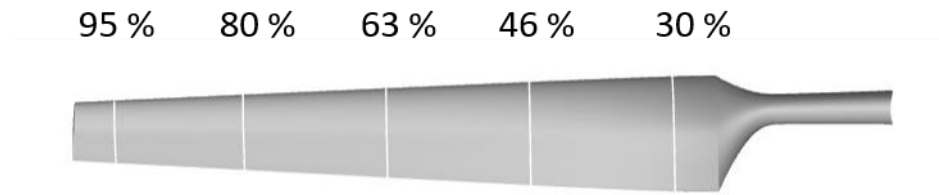


Figure 15. NREL phase VI blade with span wise sections.

Measured from the root of the blade, the span wise sections were set to 95 %, 80 %, 63 %, 46 % and 30 % of the span. The local dynamic pressures for span wise locations were calculated with Eq. (12) using facet maximum as stagnation pressure, and freestream pressure as static pressure. For the calculation of local normal forces, the blade was divided into clip sections with the length of 0.1 m. The local pressure force was calculated for x, y, and z directions using a custom field function. Total normal force was obtained by combining local pressure force and local skin friction. The force coefficient in the direction normal to the chord line was calculated using the blade twist distribution chart found in Ref. [6].

For the simulations energy equations were turned on, and turbulence model used was transition SST. Flowing air was treated as ideal gas. Blade rotation was simulated with a moving reference frame, rotating around x-axis. The rotational velocity was set to match each test scenario as in Table 1. In the boundary conditions, the far field was set as a pressure far field, inlet was set as a pressure inlet and outlet as a pressure outlet. Outlet pressure was set at atmospheric pressure. Blade walls were set as no slip walls. The rotating axis with the diameter of the hub, was set as specified shear 0 Pa wall. This was done so that the rotating axis wouldn't have friction. For pressure-velocity coupling, SIMPLEC was used. Second order discretization scheme was used.

Monitors of lift coefficient, drag coefficient and moment coefficient were set. The moment center was placed in the middle of the root of the wing. The solution was considered converged when the scaled residuals were below $10e^{-5}$, and there was no significant change in the monitors. Calculations for each wind speed were continued for approximately 20 000 iterations.

4.3 Reference wind turbine IEA-15-240

After the validation cases, the flow field around the blade of IEA-15-240 RWT was calculated. Blade geometry was obtained from Ref. [32]. The geometry of the blade needed some modifications. The rotating axis was modified to be two times bigger than the hub. This was done so that the meshing process would be easier. It was assumed that it wouldn't affect the results significantly since mainly the characteristics of the flow field closer to the tip would be interesting. A blunt surface for the blade trailing edge was made. It was assumed that the blunt trailing edge wouldn't affect the convergence of the results since it was small in comparison with the rest of the blade. For the last modification to the geometry a blunt surface to the tip was made.

Like in the validation of the NREL phase VI rotor, only one blade was simulated. Boundaries of the calculation domain were made rotationally periodic around the x-axis, and flow direction towards positive x-axis. Boundaries were set 10 diameters away from the blade upstream and downstream. In Figure 16, the entire calculation domain, and the blade in the domain are shown.

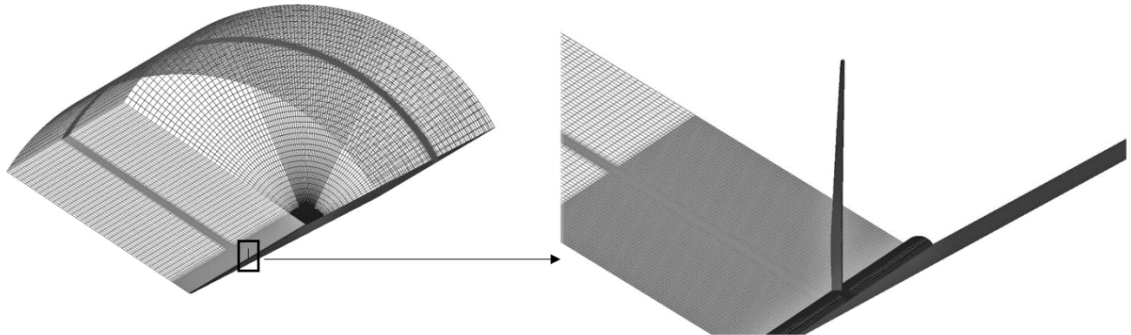


Figure 16. Entire calculation domain (left), blade in the middle of the domain (right).

The Domain was one third of a cylinder with a radius of 10 D. The blade was set with a zero degrees pitch angle. The mesh consisted of 6 million cells. The blade surface mesh was made similarly as in NREL phase VI case. O-grid was made around the blade, and first cell height was defined using y^+ calculator, and the growth factor was set to 1.2.

Simulation was made using ANSYS Fluent. Energy equation was turned on, and the turbulence model used was four equation transition SST model. A single moving reference frame with rotation around x-axis was used. Upstream and downstream boundaries were set as a pressure inlet and a pressure outlet. Pressure far field boundary condition was used for the far field. In the reference values, the turbine swept area was set as reference area, and the radius of the blade as reference length.

Two different wind speeds and rotational speeds were used in simulations. The chosen values are based on blade performance tests made with OpenFAST program. The performance table can be found in Ref. [32]. The operation conditions can be seen in Table 2.

Table 2. *IEA-15-240 RWT simulation operation conditions.*

Simulation #	1	2
Wind speed [m/s]	8.4221	5.9836
Rotor rotational speed [rpm]	8.7059	6.1851
Blade pitch angle [deg]	0.0	0.0

The wind speeds chosen for the simulations are 8.4 m/s and 8.7 m/s, and rotational velocities of 5.98 rpm and 6.18 rpm. Pitch angle was set as zero for both simulations. The wind velocities and rotor rotational speeds were chosen so that the tip speed ratio is in both cases 9.

For solver methods SIMPLEC algorithm was used for pressure-velocity coupling, and second order upwind scheme was used for spatial discretization. The Monitor for torque was set. Simulation was continued for about 25 000 iterations to ensure convergence. The result was assumed converged after scaled residuals were below $1e^{-5}$, and there was no significant variance in the monitor of torque.

4.4 Modelling impingement of water droplets on blades

In this chapter the methods for droplet trajectory, and impact calculations for 2D and 3D simulations are presented. The droplets are simulated using DPM model which uses Lagrangean particle tracking like discussed in chapter three. A one-way method is used so that droplets have no effect on the air flow, and the droplet calculations can be done in the post processing of the results.

In Chapter 2 the effects of azimuthal angle and droplet terminal velocity to the impact speed were discussed. In the droplet calculations however, the effects of gravity and azimuthal angle are ignored. To simulate those effects, it would be required to use transient solver, and it is out of scope of this work.

2D droplet modelling

For 2D droplet modelling the converged solution of IEA-15-240 RWT at 110 m radial position of the blade was used. Droplets were injected from 20 m upstream of the airfoil

to ensure that the droplets adapt fully to the flow field before they are affected by the airfoil. In total 500 droplets were released, and the release points varied from $y = -0.25$ m to $y = 0.25$ m with even spacing. The airfoil leading edge center is at $y = 0$ m, so that there would be impacts on the entire length of leading edge. The droplet trajectories are illustrated in Figure 17.

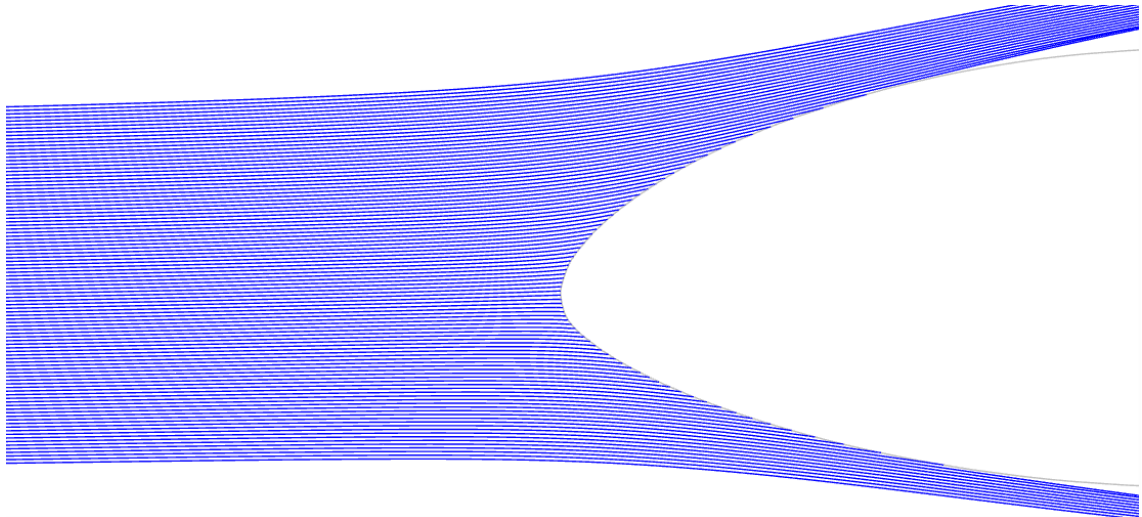


Figure 17. Droplet trajectories with impacts on the entire length of leading edge.

Each blue line resembles a particle trajectory. Between the lowest and highest impact point the average of impact speeds is calculated for each droplet diameter. Droplet density was set to 1000 kg/m^3 to resemble the density of water. The maximum number of iterations for droplets was set to 5000, and maximum error tolerance to 10^{-6} . Boundary condition for airfoil was set to trap the droplets when impacting the airfoil. Four different droplet diameters were used (0.01, 0.025, 0.5 and 0.1 mm).

Since the number of particles was high, a MATLAB code was used to write a journal that releases all the droplets, and saves text files of their velocity magnitude, velocity components and positions for x and y components. Then another MATLAB code was used to read the text files, and to determine whether there was impact or not. From the trajectories where there was an impact the maximum impact speed was calculated.

3D droplet modelling

For 3D droplet modelling the converged solution of IEA-15-240 RWT simulation was used. The droplets were released from 700 m upstream of a wind turbine and from 95 m radial position. The droplet release point in the upstream was determined by examining the contour plots of velocity to make sure that the droplets fully adapt to the surrounding flow field before they are affected by the rotor. The horizontal position of injections was

set so that particles impacted steadily to the entire length of the leading edge. The particle density was set to 1000 kg/m^3 to resemble the density of water. The same four particle diameters as in 2D simulations were used (0.01, 0.025, 0.5 and 1 mm). For each diameter 500 droplets were released.

The droplets were tracked for 18 000 iterations, and maximum error tolerance was set to 10^{-5} . High resolution particle tracking was enabled. Also, the setting to use face centroid for periodic boundaries- setting was used to minimize numerical error when particles cross periodic boundaries. Like in the 2D droplet simulations a MATLAB code was used to make a Fluent journal, which released the droplets to the flow field, and created output files for particle velocity magnitude, velocity components and position components. In Figure 18, droplet trajectories in a 3D domain are presented.

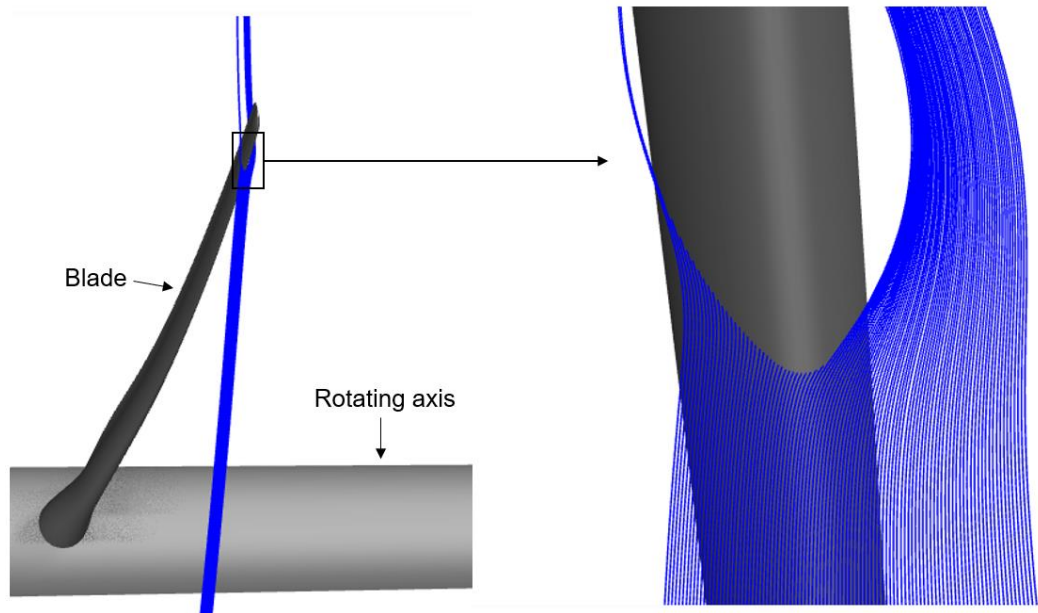


Figure 18. Droplet trajectories in 3D domain with droplets impacting the entire length of leading edge.

Each blue line resembles an individual particle trajectory, and as in the 2D case the impact speeds between the highest and lowest impact trajectory were calculated. For each droplet diameter, the average impact speed, and ratio between impact velocity and surrounding air flow velocity was calculated. The surrounding flow velocity was estimated from the components of windspeed and rotational velocity at the radial position of impact as

$$U_{flow} = \sqrt{U_{\infty}^2 + \Omega^2}, \quad (26)$$

with the ratio between impact speed and flow velocity, a fitting curve between the impact speeds of different diameter droplets was calculated. The base on which the blade

stands on the Figure 18 is the rotating axis. It has no effect on the flow and is only there to simplify the meshing.

5. RESULTS AND DISCUSSION

In this chapter, first the results for the validation of 2D and 3D simulations are presented. Then the results for the calculation of the flow field around the IEA-15-240 RWT, and comparison of results to other numerical results are presented. Lastly the droplet trajectory and impingement calculations, and comparison between 2D and 3D are presented.

5.1 Results for validation of 2D simulation

In this section, the results for mesh independence study are presented first. The number of cells in the calculation domain is closely related to the accuracy of the results. However, increasing the cell count makes the simulation more computationally demanding. The point of mesh independence study is to find the number of cells after which the flow solution does not change. After the independence study, the results for simulation cases made in this work are presented and compared with experimental wind tunnel test results from Ref. [29].

Mesh independence study was made with five mesh sizes (100 000, 150 000, 200 000, 250 000, 300 000 cells). In Figure 19, the lift coefficient with five different mesh sizes is plotted.

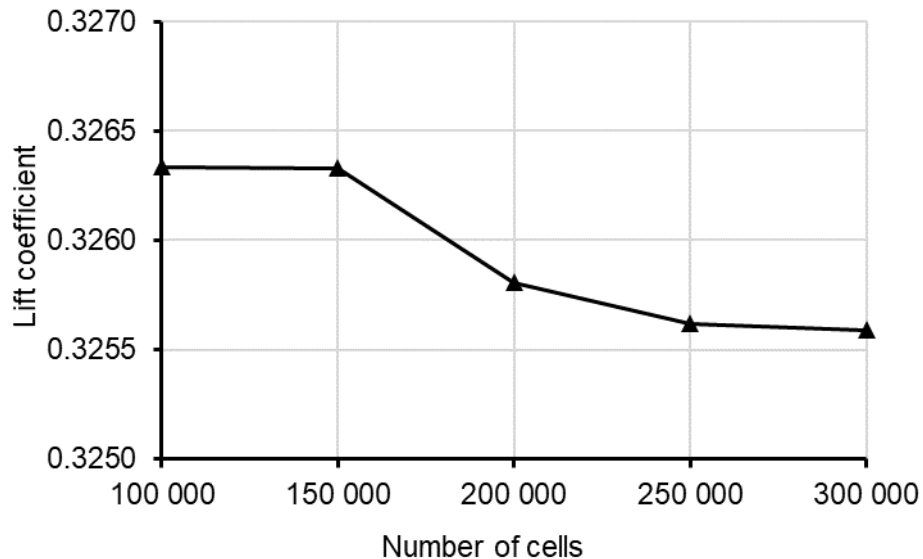


Figure 19. Mesh independence study.

The overall change in the lift coefficient is quite small from 100 000 cells to 300 000 cells with only 0.22 % decrease. In all the simulations the average y^+ on the airfoil surface was 0.2 and the maximum was 0.4. The mesh with 100 000 cells already provided nearly

mesh independent results. The mesh size of 200 000 cells was used in the 2D simulations.

In the validation of 2D simulations, the coefficients of lift, moment and drag were compared with the wind tunnel results at various angles of attack. The airfoil used was FFA-W3-211. In Figure 20, results for the moment coefficient are presented as a function of the angle of attack. In the same plot, the experimental results and results calculated with Xfoil software are plotted.

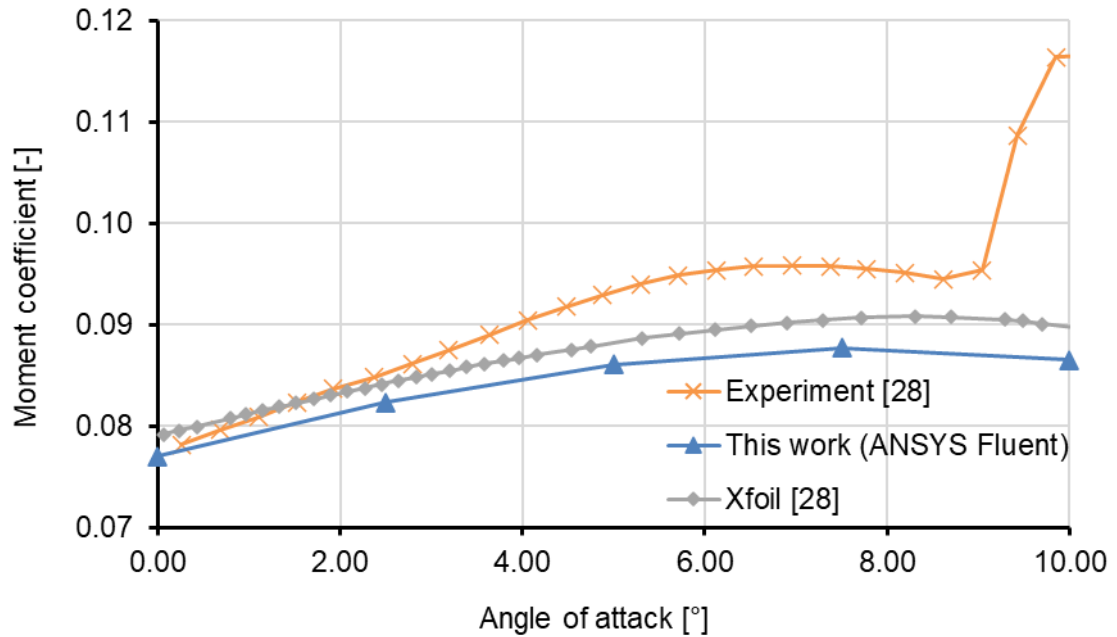


Figure 20. Moment coefficient as a function of angle of attack.

The simulation results of this work fall a bit under experimental results, and below results calculated with Xfoil. With the angle of attack of 9° the flow separation from the airfoil can be seen as the moment coefficient takes a step up in the experimental results. No similar step can be seen in the results of this work. The flow separation can't be simulated accurately with the models used in this work, and the error to the experimental values is around 35 % with the angle of attack 10°. However, before the flow separation the maximum error to the experimental values is around 9 % with the angle of attack around 6°. Error percentages of under 10 % can be considered good simulation results.

The drag coefficient was one of the values compared between experimental values and results from this work. In Figure 21, drag coefficient is plotted against the angle of attack. Again, results are compared with the experimental results and results from Xfoil simulation.

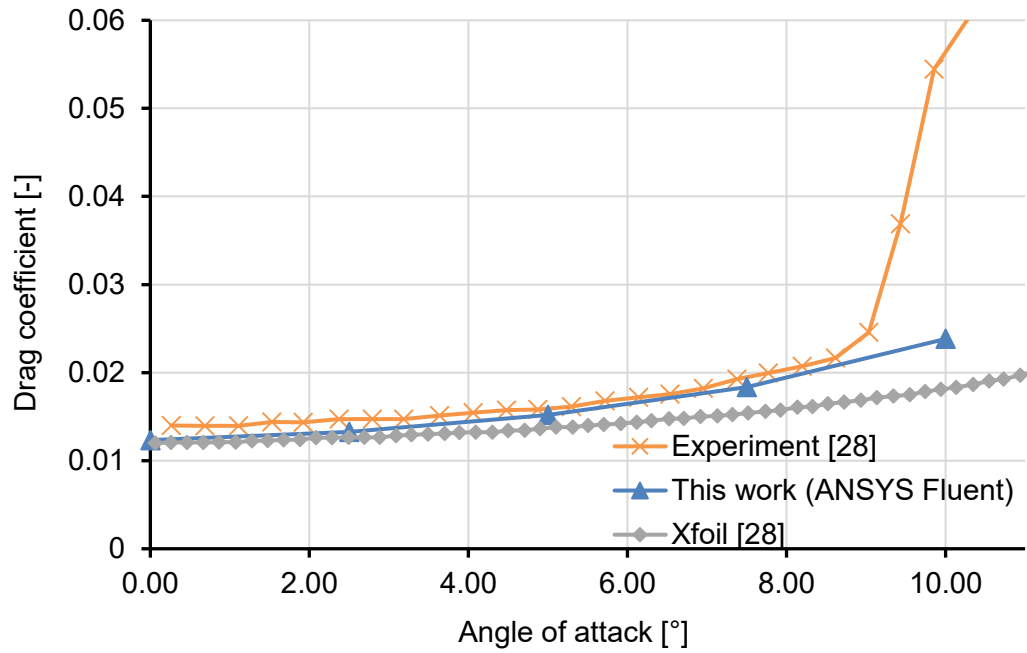


Figure 21. Drag coefficient as a function of angle of attack.

The results for drag coefficient values are between experimental and Xfoil results. Difference to the experimental results is in the range of 3-10 % when examining the conditions before the stall (around the angle of attack 9°).

The last comparison in the 2D simulations was between the lift coefficients. In Figure 22, lift coefficient is plotted against the angle of attack. With the lift coefficient, the results are compared only with the experimental values.

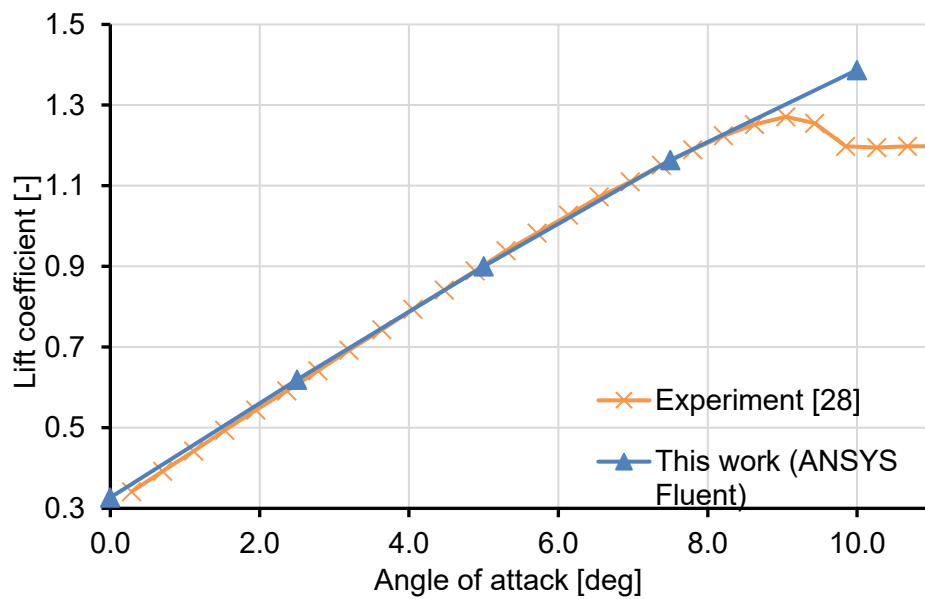


Figure 22. Lift coefficient in a function of angle of attack.

The lift coefficient follows very well with the experimental values. Excluding the stalling conditions in the high angles of attack, the maximum error is around 5 %. The results for the lift coefficient can be considered very good.

With the simulation results for the 2D validation cases presented here, it can be concluded that the simulations compare well with the experimental results. The results of this work are also in line with other similar studies. For example, Villalpando et al. [19] studied the flow field around a NACA 63-415 airfoil using ANSYS Fluent with similar models. In that study, the results of drag and lift coefficients were compared with wind tunnel data with different angles of attack. The errors to experimental results were low with the moderate angles of attack and as the angle of attack was increased above stall conditions the error increased. In this work the goal of the 2D simulation validation was to determine the models needed for an accurate prescription of a flow field around airfoil so that the droplet trajectory calculations can be made.

5.2 Results for validation of 3D simulations

In this section, the results for validating 3D simulations are presented. The goal was to find those models, that can accurately describe the flow around a wind turbine blade. The results of local normal force coefficients, local dynamic pressures and overall torque is compared with experimental results found in Ref. [6].

For the 3D validation, the experimental results of two bladed NREL Phase VI wind turbine were compared with simulation results made with ANSYS Fluent software. Results were made with several wind speeds and rotational speeds. The local values of dynamic pressures and normal force coefficients were compared with experimental values at five different span wise locations. Also, the torque values from simulations were compared with experimental values. The span wise locations where the dynamic pressures were compared are presented in Figure 23.

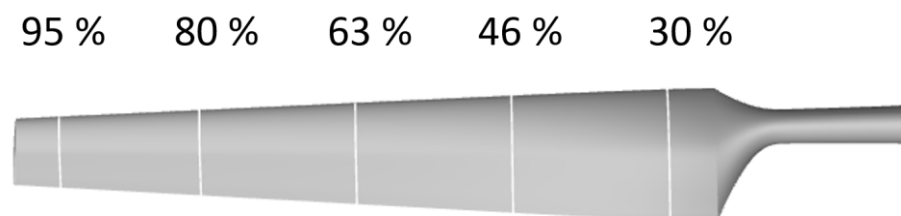


Figure 23. Span wise locations of NREL phase VI blade.

In Figure 24, the local normal force coefficients are plotted as function of wind speed with different span wise positions. By comparing the local normal force coefficients, it is possible to inspect if the values of force coefficients are consistent through the length of the blade.

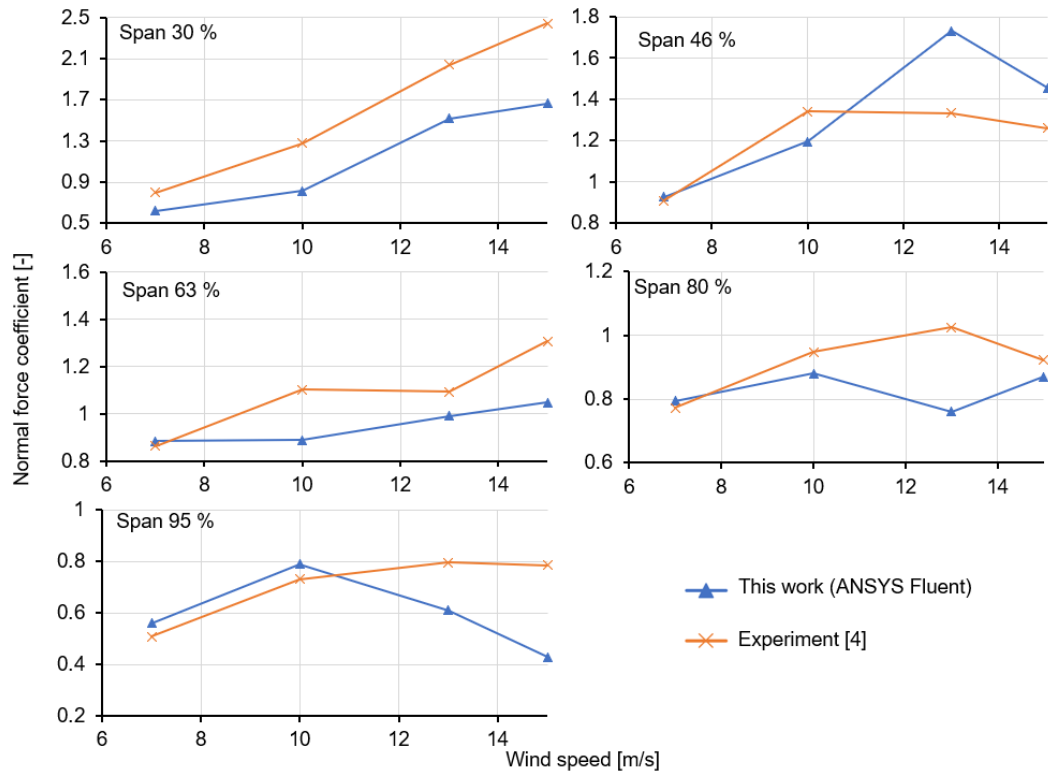


Figure 24. Local normal force coefficients [-] as a function of wind speed [m/s] for different span wise positions.

At first glance, the differences between the simulation values and the experimental values seem high. However, as seen in the 2D validation cases, the models used in this work can't predict the flow separation, which is the case with higher wind speeds. For this reason, it is possibly more reasonable to examine the results for only the lower wind speeds (7 m/s and 10 m/s). The Modelling of flow separation is not relevant in the droplet modelling point of view. In Figure 25, the local normal force coefficients and dynamic pressures are plotted as a function of span wise position with wind speeds 7 m/s and 10 m/s.

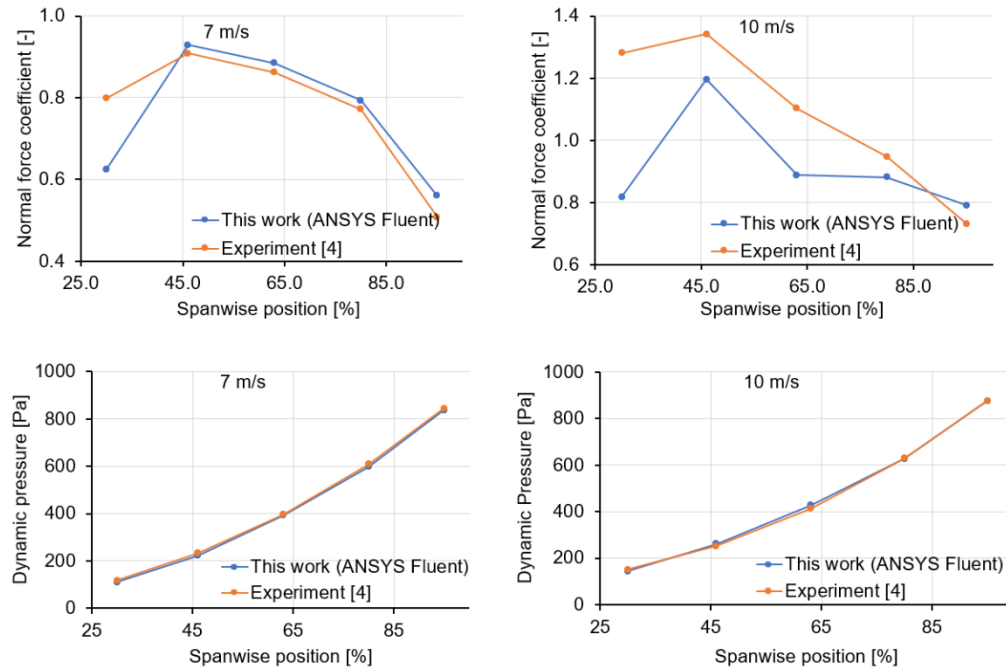


Figure 25. Local normal force coefficient [-] (top) as a function of span wise position. Local dynamic pressure [Pa] (bottom) as a function of span wise position with wind speeds 7 m/s and 10 m/s.

On the left side of Figure 25, the values of local normal force coefficients (on top) and local dynamic pressures (bottom) are presented with 7 m/s wind speed case, and on the right side with 10 m/s wind speed case. The normal force coefficient has an error of about 28 % with the 7 m/s case and 56 % with 10 m/s case in the span wise position closest to the blade root. Both errors are quite high, especially when comparing with the rest of the rest of the error percentages in 7 m/s case which is in the range of 2-9 %. The high error in the blade section closer to the root can be explained with the blade geometry. The local angle of attack is probably too high closer to the root due to structural limitations of the blade, and because of this there is some flow separation in the root section. The error values of the normal force coefficient in the 10 m/s case, when excluding the first span wise position, is in the range of 7-25 %. The values are in quite good agreement with the experimental values, but with this wind speed the flow starts to separate from the wing also in other span wise locations. The local dynamic pressures show very little variation to experimental values in both wind speed cases. The percentage is about 6.5 % at the highest.

In Figure 26, the contours of turbulent kinetic energy are presented in the span wise sections of the blade. The contours are taken from the 7 m/s and 10 m/s simulation cases.

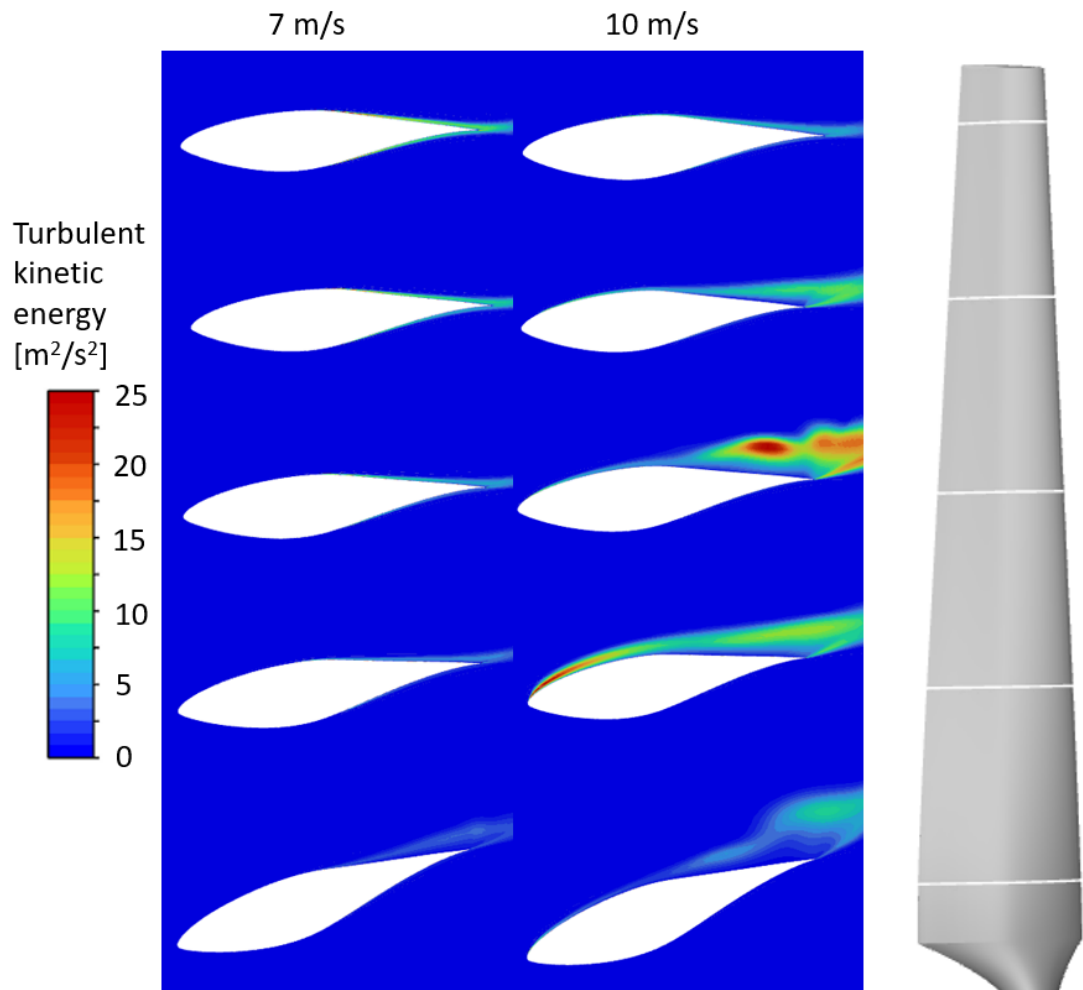


Figure 26. Contours of turbulent kinetic energy in the span wise locations of the wing.

The turbulent kinetic energy rises as the wind speed rises, and the flow starts to separate from the blade. The turbulent kinetic energy is at the highest in the 46 % and 63 % of the span wise positions in the 10 m/s case, whereas in the same positions in the 7 m/s case there is no considerable amount of turbulent kinetic energy. This is well in line with the error values of normal force coefficients, which were the highest at these blade positions.

The overall torque of the rotor was one of the values compared between simulation results and experimental results. In Figure 27, torque of the blades is presented as a function of wind speed. Since the simulations were made with only one blade, taking advantage of periodicity, the values of torque have been multiplied by two to resemble the overall torque of two bladed rotor.

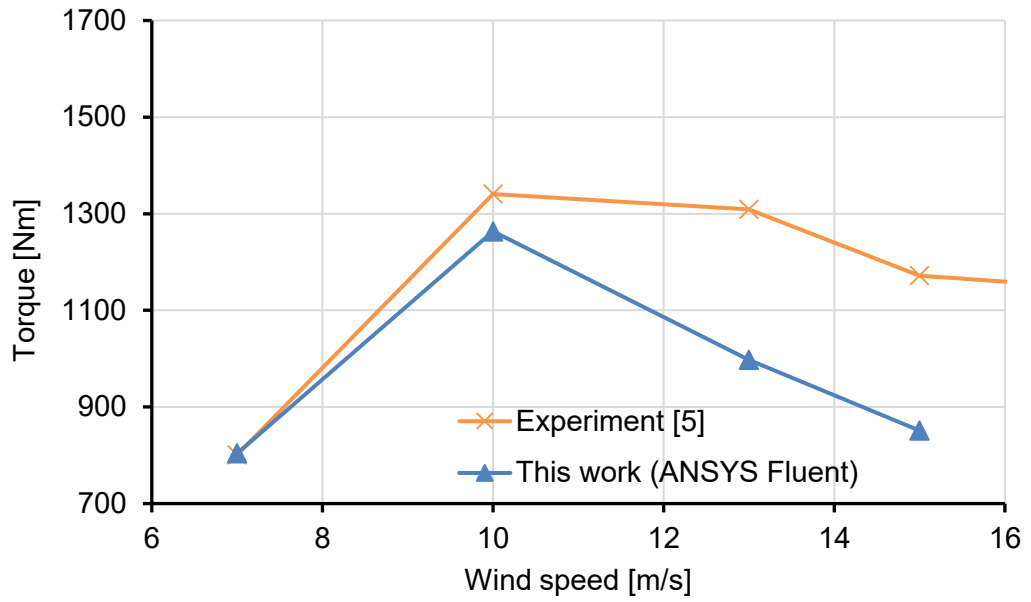


Figure 27. Torque as function of wind speed.

With the values of torque, the trend is very similar as in the results listed above. With lower wind speeds, the simulation results compare well with the wind tunnel tests, and as the wind speed increases the error between results grow. In the cases of wind speed 13 m/s and 15 m/s, Fluent under predicts the torque values significantly. In Table 3, percentage error of torque values is presented.

Table 3. Error percentage of torque values.

Wind speed [m/s]	7	10	13	15
Error %	0.35	-5.77	-23.79	-27.37

With the 7 m/s case the value of torque is almost the same as the experimental value with only 0.35 % error. In the 10 m/s case the error is still reasonable with about 6 %, and with 13 and 15 m/s cases the error very rapidly increases. The Fluent simulation results are all below the experimental values, except with the 7 m/s case which has practically no error at all.

The purpose of the validation cases, both in 2D and in 3D, was to make sure that the simulation results correspond accurately enough with the experimental values. Accurate simulation of the flow field around the blade works as foundation for droplet simulations, and therefore the accuracy of droplet simulations greatly depends on the flow solution. The results for validation cases can be considered expected and successful. The limitations of models used in this work are in line with other studies made with similar models Ref. [20] and Ref. [21]. Limitation of the models used here are the incapability to model flow separation accurately. With low wind speeds, the simulation results compare well

with the experimental results. For the droplet simulations the operation conditions should be selected so that there is no considerable amount of flow separation to ensure the accuracy of the simulations.

5.3 Results for IEA-15-240-RWT

In this section, the results simulating the flow field around the reference wind turbine IEA-15-240 are presented and compared with other numerical results since no experimental data is available. The droplet trajectories will be calculated in this flow field, so it is important that the simulated flow field is as accurate as possible.

The flow field for IEA-15-240-RWT was calculated with two different wind speeds 8.4 m/s and 8.7 m/s. Rotor rotational speed for the 8.4 m/s case was 5.98 RPM and for the 8.7 m/s case 6.18 RPM. Since there was no experimental data available, the results were compared with numerical results obtained with OpenFAST program, which is based on BEM method. The OpenFAST results can be found in Ref. [32]. The comparison of aerodynamic forces and moments for wind speed 8.4 m/s are shown in Table 4.

Table 4. *Results for wind speed 8.4 m/s.*

	OpenFAST [28]	This Work (ANSYS FLUENT)	Difference %
rotor thrust [MN]	1.54	1.52	-0.69
rotor torque [MN]	12.3	12.7	2.86
flap wise bend [MNm]	40.9	41.2	0.82
power coefficient [-]	0.464	0.474	2.30
thrust coefficient [-]	0.776	0.766	-1.16
torque coefficient [-]	0.0518	0.0527	1.86

The comparison between OpenFAST and simulation results for wind speed 8.7 m/s is presented in Table 5. The error is very low for every measured value. Both the results are obtained with numerical methods, so they are expected to be similar. With ANSYS Fluent, all the results are overestimated when comparing with the OpenFAST results, except the rotor thrust.

In Table 5, the simulation results for wind speed 8.7 m/s are presented with the OpenFAST results and the difference between them. Two different wind speeds were chosen to make sure that the results are consistent.

Table 5. *Results for wind speed 8.7 m/s.*

	OpenFAST [28]	This Work (ANSYS FLUENT)	Differ- ence %
rotor thrust [MN]	1.64	1.63	-0.48
rotor torque [MN]	13.2	13.6	3.32
flap wise bend [MNm]	43.7	44.2	1.08
power coefficient [-]	0.464	0.474	2.27
thrust coefficient [-]	0.776	0.764	-1.47
torque coefficient [-]	0.0518	0.0527	1.78

With the case with slightly increased wind speed and rotor rotational speed the values compare again very well with the OpenFAST results. With both wind speeds, the difference between OpenFAST results and the results for this work. The thrust value was slightly underpredicted while the rest of the values slightly overpredicted by the simulations made in this work. Overall, both simulation cases can be considered very successful and can be used as a foundation for droplet simulation calculations.

5.4 Droplet impact speeds and comparison of 2D and 3D results

In this section, the results for droplet trajectory and impact calculations are presented. The main goal of this study was to study the droplet trajectories and impact speeds in 2D and 3D simulations, and to provide impingement data which can be used in an erosion model.

For the droplet trajectory calculations, IEA-15-240 RWT was used. Droplets with the density of 1000 kg/m^3 and diameters of 0.1, 0.25, 0.5 and 1 mm were calculated for 2D and 3D cases. 500 droplets were released for each diameter. In Figure 28, average particle impact speed relative to the upstream velocity as a function of droplet diameter is presented.

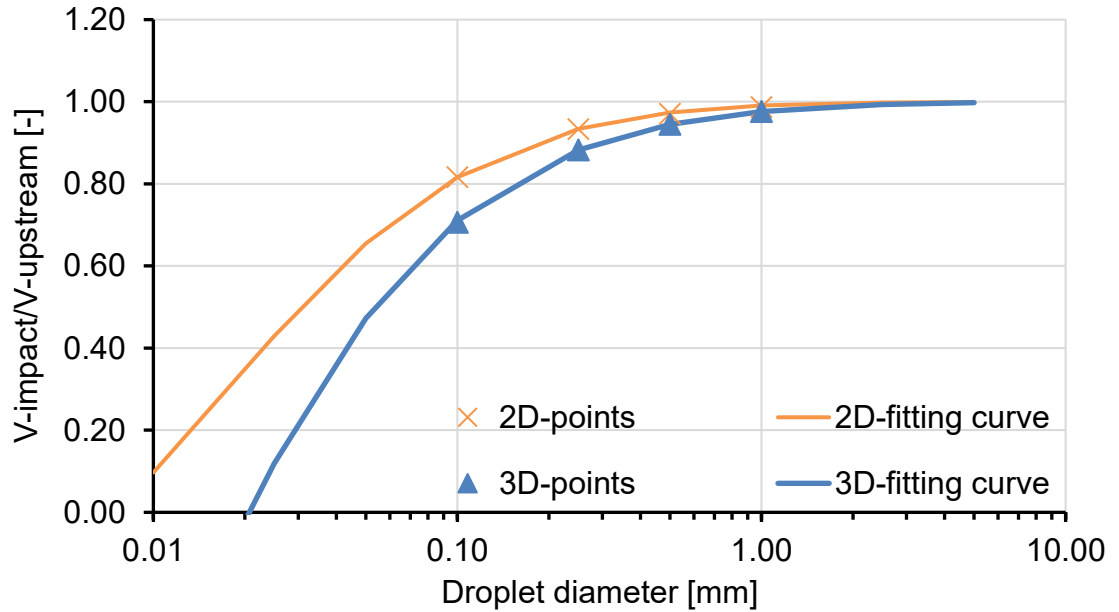


Figure 28. Average impact speed relative to upstream velocity as a function of droplet diameter.

With the 3D simulation, the impact speeds of droplets are lower than in 2D simulation. However, as the diameter of the droplets increases the differences in impact speeds gets smaller. In the 2D simulations, the upstream velocity is the inlet velocity. In the 3D simulation, the upstream velocity of the impact position depends on the wind speed and the radial speed of the blade in that position. The upstream velocity for 3D droplets has been calculated with Eq. (26) using average of the radial positions of each droplet diameter. Then this local radial velocity has been used as inlet velocity for the 2D simulation.

The radial position of impact varied approximately 2 meters between different diameters of droplets. The biggest droplets impact at the lowest of the blade. This is because they are not as easily adapted by the flow as the smaller droplets. With the same diameter droplets, the standard deviation of the radial position of impact was in between 0.01-0.02. Since the standard deviation was very small, the use of average position when determining the local upstream velocity, probably didn't have much impact on the results.

When examining the impact positions of maximum impact velocities, it was noted that the maximum impact velocities were on the suction side of the airfoil. This is probably due to the flow accelerating on the upper side of the airfoil. In Figure 29, comparison of impact positions of maximum impact speeds is presented.

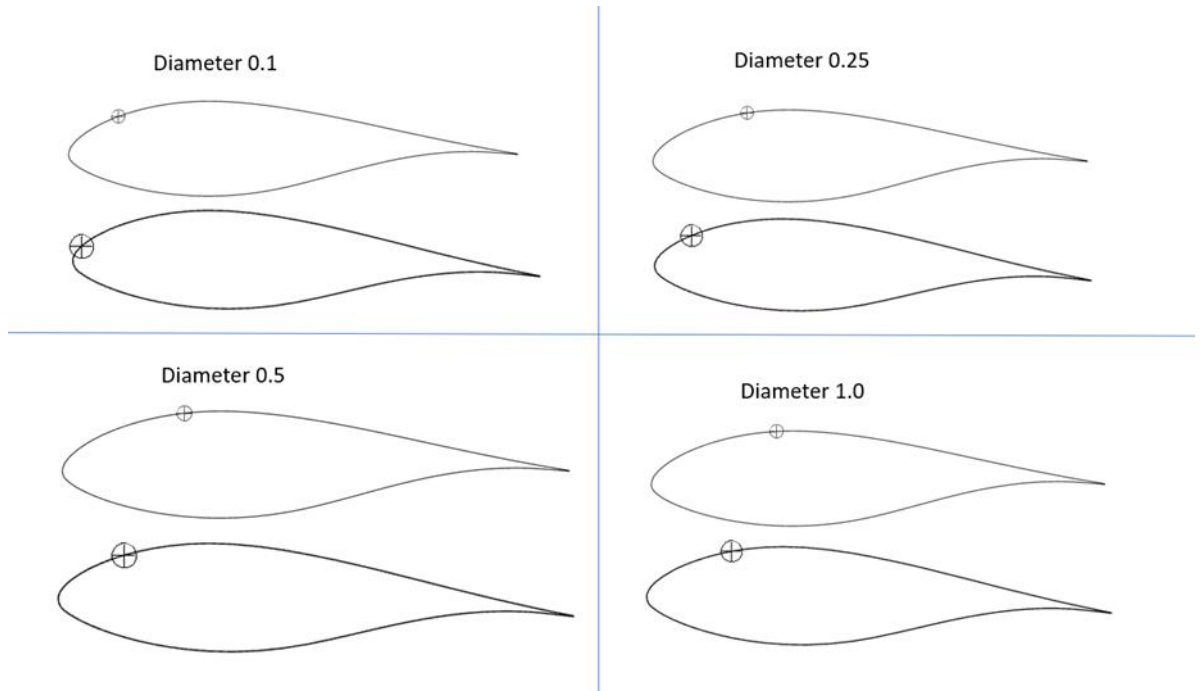


Figure 29. Comparison of positions of maximum impact velocity positions in 2D and 3D simulations with different diameter droplets. Droplet diameter in mm. (2D impact position on top and 3D below).

The maximum impact velocities are further on the suction side in the 2D simulations than in the 3D simulations. Also, for both 2D and 3D simulations, the maximum impact velocity point is the furthest on the suction side with the biggest droplets, and closest to the leading edge with the smallest droplets. These droplets impacting on the suction side of the airfoil are probably not the most relevant for erosion, since the impact angle is low. It would probably have been better to exclude from the impact speed calculations the trajectories that impact on the upper or on the lower side of the airfoil, and only inspect the more direct impacts. The difference in maximum velocity impact points can probably at least partly be explained with the angle of attack. The 2D simulation has the zero angle of attack whereas the 3D simulation has the angle of attack greater than zero.

In Figure 30, velocity contours of both simulations are presented. On the left side of the figure the velocity contour of 2D simulation is presented, and on the right side the velocity contour of 3D simulation at the radial position of 110 m of the blade. This radial position is the same as the impact position of the smallest particles (0.1 mm).

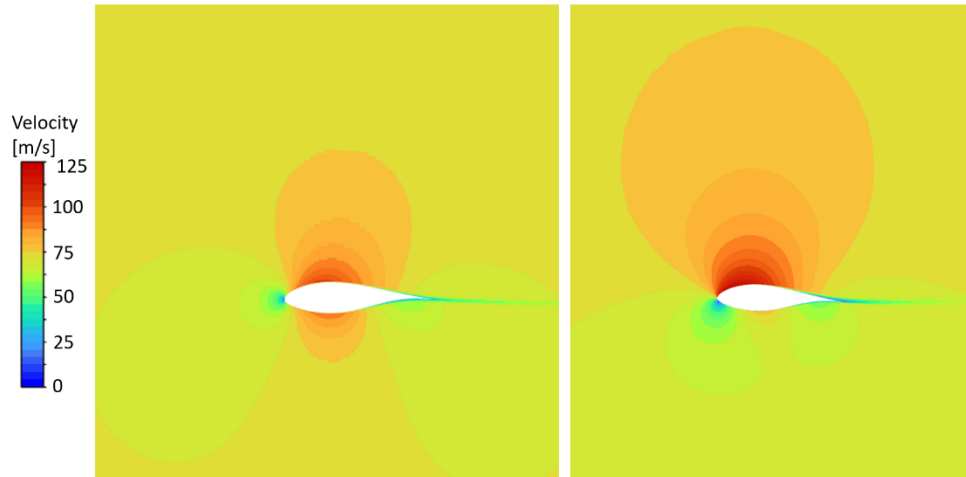


Figure 30. Velocity contours of 2D simulation (left) and the 3D simulation (right) at the radial position of impingement.

From the contour plots, the differences in velocity fields between 2D and 3D cases can be seen. The surrounding flow velocity seems to be quite the same in both cases, and that the approximation for inlet velocity for the 2D simulation matches well the velocity of 3D simulation. However, the velocities on the upper and lower side are higher in the 3D simulation than in the 2D simulation. Also, the different angle of attack can be seen in the pictures with the stagnation point (the blue circle at the leading edge where velocity is zero) on the leading edge being more on the lower side on the airfoil in the 3D simulation. This probably explains why the impact positions are further on the suction side in 2D simulations than in 3D simulations. The lower impact speeds, especially with smaller particles, can also be explained with the angle of attack. The droplets reaccelerate when they are passing the airfoil in both 2D and 3D cases, but rather than impacting they bypass the airfoil when the angle of attack is high.

6. CONCLUSIONS AND FUTURE WORK

In this work, the aerodynamics of a wind turbine blade, and droplet impingement on the blade were simulated using ANSYS Fluent software. The thesis work consisted of validation of the results for the aerodynamic forces and moments of 2D and 3D simulations by comparing the results with existing wind tunnel data. After the validation of results the droplet trajectories and impact speeds were calculated. The purpose of this work was to simulate the droplet trajectories and impact speeds in 2D and 3D simulations, and to compare the results with each other, and to produce impingement data which can later be used in a blade erosion model.

The first research question was to clarify the aerodynamic properties of a wind turbine, and how they are connected to the droplet impingement and erosion of the blades. As air flows around a wind turbine blade, it generates a lift that rotates the blades. Rotating blades also affects the flow field around the blade. The erosion of the blades depends on the impact speed of droplets. The impact speed of a droplet impinging on a wind turbine blade depends on the terminal velocity of droplet and rotor rotational speed. The size of a droplet also affects the impact speed since the smaller droplets tend to get adapted by the rotor induced flow field faster than the larger droplets. This means that smaller droplets might not even hit the blade since they flow around it with the airflow, whereas the trajectory of a larger droplet is more similar to a straight line.

The second research question was to solve the simulation strategies and sub models needed to model the flow around a wind turbine blade as accurately as possible but with a moderate computational cost. A steady state solver was used in this work, and the rotation of the blades was simulated using a moving reference frame, which was chosen based on similar studies. Flow around wind turbine blades have been studied extensively with CFD tools, and it was found out that $k - \omega$ SST and transition $k - \omega$ SST turbulence models are the most suitable options for wind turbine simulations in the accuracy and computational cost point of view.

The third research question was to compare the simulation results of this work with existing wind tunnel data. For 2D simulations FFA-W3-211 airfoil, and for 3D NREL Phase VI blade was used. It was found out that the simulation results compare well with the wind tunnel data with both 2D and 3D simulations if there was no considerable amount of flow separation from the wing. In the 2D simulations, the simulation results for lift coefficients were in the range of 5 % with the angles of attack 0° , 2.5° , 5° and 7° when

comparing with the experimental results. After increasing the angle of attack above 7° , error rapidly increased. Similar behavior was seen in the results of 3D simulations with the torque values being within 5 % of the experimental data for 7 m/s and 10 m/s wind speeds. With the wind speeds of 13 m/s and 15 m/s the error was around 25 %.

The fourth research question was about droplet impingement on the IEA-15-240 reference wind turbine blade. The aim was to clarify the droplet trajectories and impact speeds, and to compare the results of 2D and 3D simulations. Droplet simulations were made with DPM model. The droplet impact speeds and trajectories behaved as expected with the impact speed being lower than the upstream velocity since the droplets are affected by the rotor induced flow field. With the smaller droplets, the impact speeds were lower than with larger droplets since they are adapted by the surrounding flow faster. Also, in the 3D simulations it was seen that the radial position of impact was higher than the release point of the droplets. This can be explained with the stream tube of airflow expanding as it approaches the turbine. The difference between the 2D and 3D cases were that in the 2D simulations the impact speeds were higher with all the droplet sizes used in this work. The differences may be at least partly explained with the different angle of attack used in the 2D simulations than in 3D simulations. Also, the method of calculating the upstream velocity may have affected the results in the 3D cases since the velocity was calculated using components of wind speed and rotational velocity, because the rotational velocity changed with the changing radial position of the impact.

For the future work, the particle impingement model could be improved. The model could be modified to calculate the impact speeds of particles impacting directly to the leading edge and exclude the ones with a low impact angle. The angle of attack in the 2D simulation should be fixed to be the same as in the impact positions of 3D simulation. The local angle of attack could be estimated for example by evaluating pressure coefficient curves in the position of impact and trying to find the angle of attack with a matching pressure coefficient curve. Also, the droplet trajectory simulations could be expanded to include particles with different densities and more diameters.

REFERENCES

- [1] R. Herring, K. Dyer, F. Martin, C. Ward, The increasing importance of leading edge erosion and a review of existing protection solutions, *Renewable & sustainable energy reviews*, Vol.115, 2019.
- [2] IEA, Wind electricity, International Energy Agency, Paris, 2022, Available (accessed, 22.12.2022): <https://www.iea.org/reports/wind-electricity>
- [3] J.F. Manwell, J.G. McGowan A.L. Rogers, *Wind energy explained: theory, design and application*, Wiley, 2nd ed. Chichester, United Kingdom, 2009, 689 p.
- [4] A. Sareen, C.A. Sapre, M.S. Selig, Effects of leading edge erosion on wind turbine blade performance: Effects of leading edge erosion, *Wind Energy*, Chichester, Vol.17, pp. 1531–1542.
- [5] T. Burton, D. Sharpe, N. Jenkins, E. Bossanyi, *Wind energy handbook*, Wiley, Chichester, England, 2001, 617 p.
- [6] J.M. Jonkman, Modeling of the UAE Wind Turbine for Refinement of FAST_AD, National renewable energy laboratory, Colorado, 2003,
- [7] F.M. White, *Fluid mechanics*, McGraw Hill, 8th ed. New York, 2015, 848 p.
- [8] J. Anderson, *Fundamentals of Aerodynamics*, McGraw Hill, 6th ed. New York, 2017, 1130 p.
- [9] E. Hau, *Wind Turbines: Fundamentals, Technologies, Application, Economics*, Springer, 1st ed. Berlin, 2000, 624 p.
- [10] J. Chen, Q. Wang, *Wind turbine airfoils and blades: optimization design theory*, De Gruyter, Berlin, 2018, 392 p.
- [11] A.R. Radmanesh, M. Abbaspour, M.R. Soltani, Unsteady Aerodynamic Analysis of Different Multi-MW Horizontal Axis Wind Turbine Blade Profiles on SST K- ω Model, Exergy for a better environment and improved sustainability: FUNDAMENTALS, Cham: Springer International Publishing, 2018, pp. 17–30.
- [12] R. Herring, K. Dyer, P. Howkins, C. Ward, Characterisation of the offshore precipitation environment to help combat leading edge erosion of wind turbine blades, *Wind energy science*, Vol.5, No. 4, 2020, pp. 1399–409.
- [13] J.I. Bech, C.B. Hasager, C. Bak, Extending the life of wind turbine blade leading edges by reducing the tip speed during extreme precipitation events, *Wind energy science*, Vol.3, No. 2, 2018, pp. 729–748.
- [14] A. Kubilay, D. Derome, B. Blocken, J. Carmeliet, CFD simulation and validation of wind-driven rain on a building facade with an Eulerian multiphase model, *Building and environment*, Vol.61, 2013, pp. 69–81.
- [15] R. Gunn, G. Kinzer, The terminal velocity of fall for water droplets in stagnant air, *Journal of meteorology*, Vol. 6, No. 4, 1949, pp. 243–248.
- [16] R. Prieto, T. Karlsson, A model to estimate the effect of variables causing erosion in wind turbine blades, *Wind Energy*, Vol.24, No. 9, 2021, pp.1031-1044.

- [17] H.K. Versteeg, W. Malalasekera, *An introduction to computational fluid dynamics: The finite volume method*, Pearson Education, 2nd ed., Harlow, 2007, 503 p.
- [18] ANSYS Inc., *Ansys Fluent Theory Guide*, Canonsburg, 2022, <http://www.ansys.com>.
- [19] F. Villalpando, M. Reggio, A. Ilinca, *Assessment of Turbulence Models for Flow Simulation around a Wind Turbine Airfoil*, *Modelling and simulation in engineering*, Vol.2011, 2011, pp. 1–8.
- [20] B. Ji, K. Zhong, Q. Xiong, P. Qiu, X. Zhang, L. Wang, *CFD simulations of aerodynamic characteristics for the three-blade NREL Phase VI wind turbine model*, *Energy (Oxford)*, Vol.249, 2022.
- [21] E. Sagol, M. Reggio, A. Ilinca, *Assessment of Two-Equation Turbulence Models and Validation of the Performance Characteristics of an Experimental Wind Turbine by CFD*, *ISRN Mechanical Engineering*, Vol.2012, 2012, pp. 1–10.
- [22] A.R. Sudhamshu, M.C. Pandey, N. Sunil, N.S. Satish, V. Mugundhan, R.K. Velamati, *Numerical study of effect of pitch angle on performance characteristics of a HAWT*, *Engineering science and technology an international journal*, Vol.19 No. 1, 2016, pp. 632–641.
- [23] J.O. Mo, Y.H. Lee, *CFD Investigation on the aerodynamic characteristics of a small-sized wind turbine of NREL PHASE VI operating with a stall-regulated method*, *Journal of mechanical science and technology*, Vol.26 No. 1, 2012, pp. 81–92.
- [24] N.S. Tachos, A.E. Filios, D.P. Margaritis, *A comparative numerical study of four turbulence models for the prediction of horizontal axis wind turbine flow*, *Proceedings of the Institution of Mechanical Engineers. Part C. Journal of mechanical engineering science*, Vol.224, No. 9, 2010, pp. 1973–1979.
- [25] M.A. Elfarra, N. Sezer-Uzol, I.S. Akmandor, *NREL VI rotor blade: numerical investigation and winglet design and optimization using CFD*, *Wind Energy (Chichester)*, Vol.17, No. 4, 2014, pp. 605–626.
- [26] M. Moshfeghi, Y.J. Song, Y.H. Xie, *Effects of near-wall grid spacing on SST-K- ω model using NREL Phase VI horizontal axis wind turbine*, *Journal of wind engineering and industrial aerodynamics*, Vol.107-108, 2012, pp. 94–105.
- [27] C. Yang, G. Tong, *Numerical computation and analyses on the blade aerodynamic performance of a horizontal axis wind turbine rotor*, *Asia-Pacific power and energy engineering conference (APPEEC)*, 2011, pp. 1-4.
- [28] *NREL transforming energy: OpenFAST*, National Renewable Energy Laboratory, Available (accessed 11.11.2022): <https://www.nrel.gov/wind/nwtc/openfast.html>
- [29] F. Bertagnolio, N. Sørensen, J. Johansen, P. Fuglsang, *Wind turbine airfoil catalogue*, Risø National Laboratory, Roskilde, Denmark, 2001.
- [30] A. Björk, *Coordinates and calculations for the FFA-W1-xxx, FFA-W2-xxx AND FFA-W3-xxx series of airfoils for horizontal axis wind turbines*, The Aeronautical Institution of Sweden, Stockholm, 1990.
- [31] ANSYS Inc., *Ansys Fluent User's Guide*, Canonsburg, 2022, <http://www.ansys.com>.
- [32] IEA Wind, *IEA-15-240-RWT*, National Renewable Energy Laboratory, Available (accessed 15.10.2022): <https://github.com/IEAWindTask37/IEA-15-240-RWT>